Performance Enhancement of Linear Scanned Arrays through an Innovative Material-by-Design Methodology

M. Salucci, G. Oliveri, N. Anselmi, G. Gottardi, and A. Massa

Abstract

A novel quasi conformal transformation optics (*QCTO*)-based approach is introduced for the synthesis of coating meta-lenses that are able to improve the radiation pattern of the covered linear antenna arrays. Thanks to the *QCTO* technique, the proposed material-by-design synthesis methodology is able to reduce the half-power beam-width (*HPBW*) and the side-lobe level (*SLL*) of a given linear array without introducing strong anisotropies in the synthesized meta-material coating lens. Some representative numerical examples are shown in order to assess the effectiveness, as well as the limits, of the proposed *MbD* method.

1 Half-Gauss Profile - $h' = 4.0$ [λ], $l' = 1.0$ [λ], $t' = 10.0$ [λ], $N = 15$ - Analysis vs. w'

1.1 Step 1: Expanding the physical array ($N = 15$, $L = 7.0$ [λ])

Input Parameters

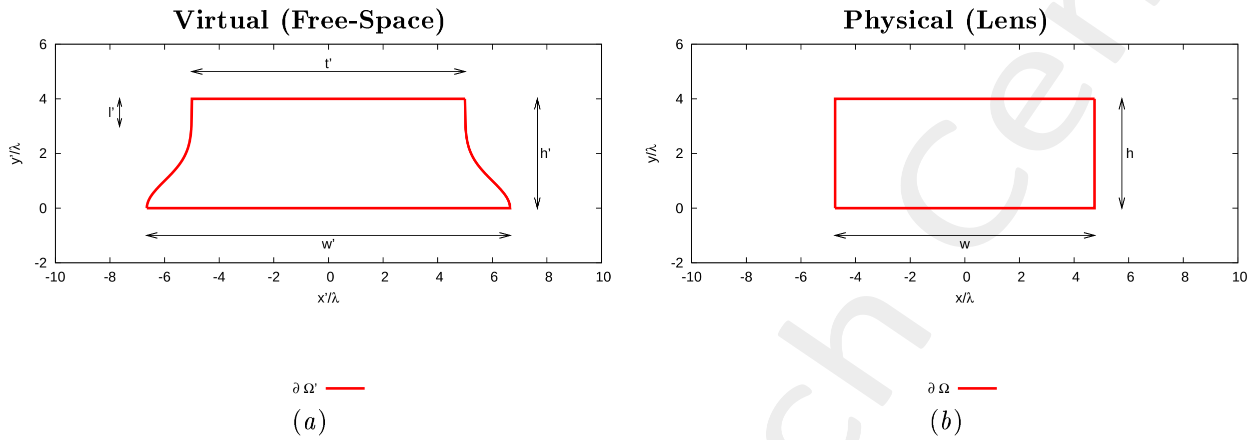

Figure 1: Transformation regions. The lower side of both virtual and physical boundaries are supposed to be PEC.

- **Virtual Geometry**

  NOTE: the left and right sides of the virtual domain are composed by two half-Gaussian shapes. For both sides, the Gaussian shape has been generated within the range $[0, 3\sigma]$, where the standard deviation has been set equal to $\sigma = (h' - l')$.

# Test Case	h' [λ]	l' [λ]	t' [λ]	w' [λ]
1	4.0	1.0	10.0	**10.8**
2	4.0	1.0	10.0	**11.5**
3	4.0	1.0	10.0	**12.1**
4	4.0	1.0	10.0	**12.7**
5	4.0	1.0	10.0	**13.3**

Table I: Considered virtual geometries. The values of w' have been empirically determined in order to achieve an aperture of the virtual array (L') equal to a multiple of $\lambda/2$. It is imposed that $h = h'$, while w is not controlled by the user.

- **Physical Array**
  - Number of elements, spacing, aperture: $N = 15$, $d = \frac{\lambda}{2}$, $L = 7.0$ [λ];
  - Positions: $x_n \in [-L/2, L/2]$, $y_n = \frac{\lambda}{4}$, $n = 1, ..., N$;
  - Steering angle: $\phi_s = 90.0$ [deg];
  - Excitations: $I_n = 1.0$, $\varphi_n = \frac{-2\pi}{\lambda} x_n sin(\phi_s + 90)$; $n = 1, ..., N$;

- **QCTO**
  - Discretization cell dimension: 0.15 [λ] (0.01 [λ] for source mapping);

1.1.1 Results

Transformation grids

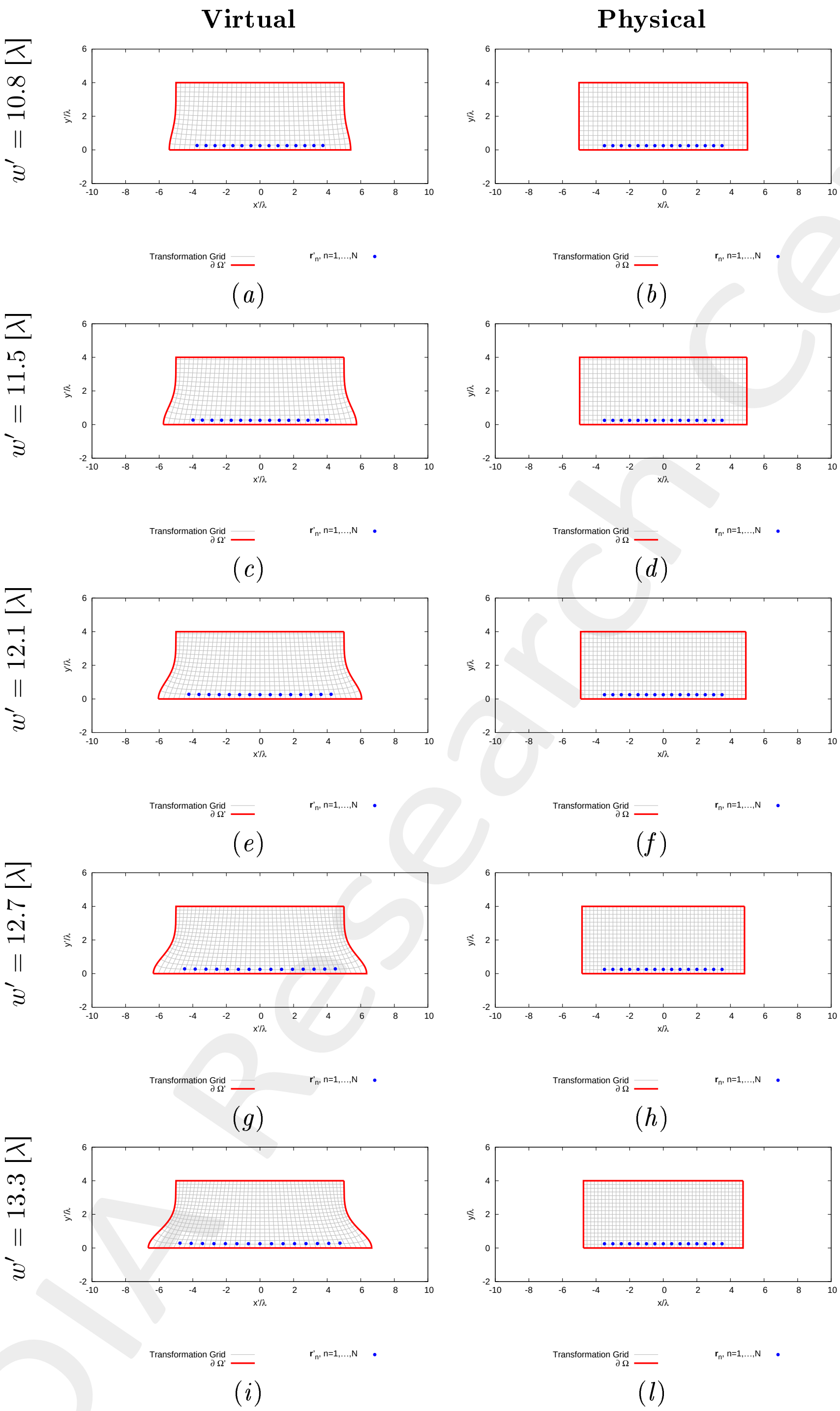

Figure 2: Transformation grids for different values of w'. Physical geometry has been shifted on y by $h/2 = 2.0$ [λ].

Resulting aperture of the virtual array (L') - for step 2

- The aperture of the virtual array (L') is computed after mapping the physical array into the virtual space;
- The resulting number of equi-spaced elements is computed as

$$N' = round\left(\frac{L'}{0.5} + 1\right)$$

	Virtual Geometry				**Virtual Array**	
# Test Case	h' [λ]	l' [λ]	t' [λ]	w' [λ]	L' [λ]	N'
1	4.0	1.0	10.0	**10.8**	7.49	**16**
2	4.0	1.0	10.0	**11.5**	7.98	**17**
3	4.0	1.0	10.0	**12.1**	8.46	**18**
4	4.0	1.0	10.0	**12.7**	8.97	**19**
5	4.0	1.0	10.0	**13.3**	9.53	**20**

Table II: Resulting aperture and number of equi-spaced elements of the virtual array after expanding the physical array.

Observations

- With respect to the half-cosine geometry (using the same values for h', l' and t'), it seems that this geometry provides larger extensions of the original physical array with lower values of w'.
- However, since the size of the lens (i.e., its width, w) cannot be controlled, we cannot say a-priori that the compression between virtual and physical domains will be lower thanks to lower values of w' (with the main consequence of raising lower values of the permittivity/permeability physical tensors).

1.2 Step 2: Compressing the virtual array ($N' > N$, $L' > L$ [λ])

Input Parameters

- **Virtual Array**
  - Number of elements, spacing, aperture: $N' = \{16; 17; 18; 19; 20\}$, $d' = \frac{\lambda}{2}$, $L' = \{7.5; 8.0; 8.5; 9.0; 9.5\}$ [λ];
  - Positions: $x'_n \in [-L'/2, L'/2]$, $y'_n = \lambda/4$, $n = 1, ..., N'$;
  - Steering angle: $\phi_s = 90.0$ [deg];
  - Excitations: $I'_n = 1.0$, $\varphi'_n = \frac{-2\pi}{\lambda} x_n sin\,(\phi_s + 90)$; $n = 1, ..., N'$;
- **Virtual Geometry:** same of step 1;
- **QCTO:** same of step 1.

1.2.1 Results of the Transformation

Transformation grids

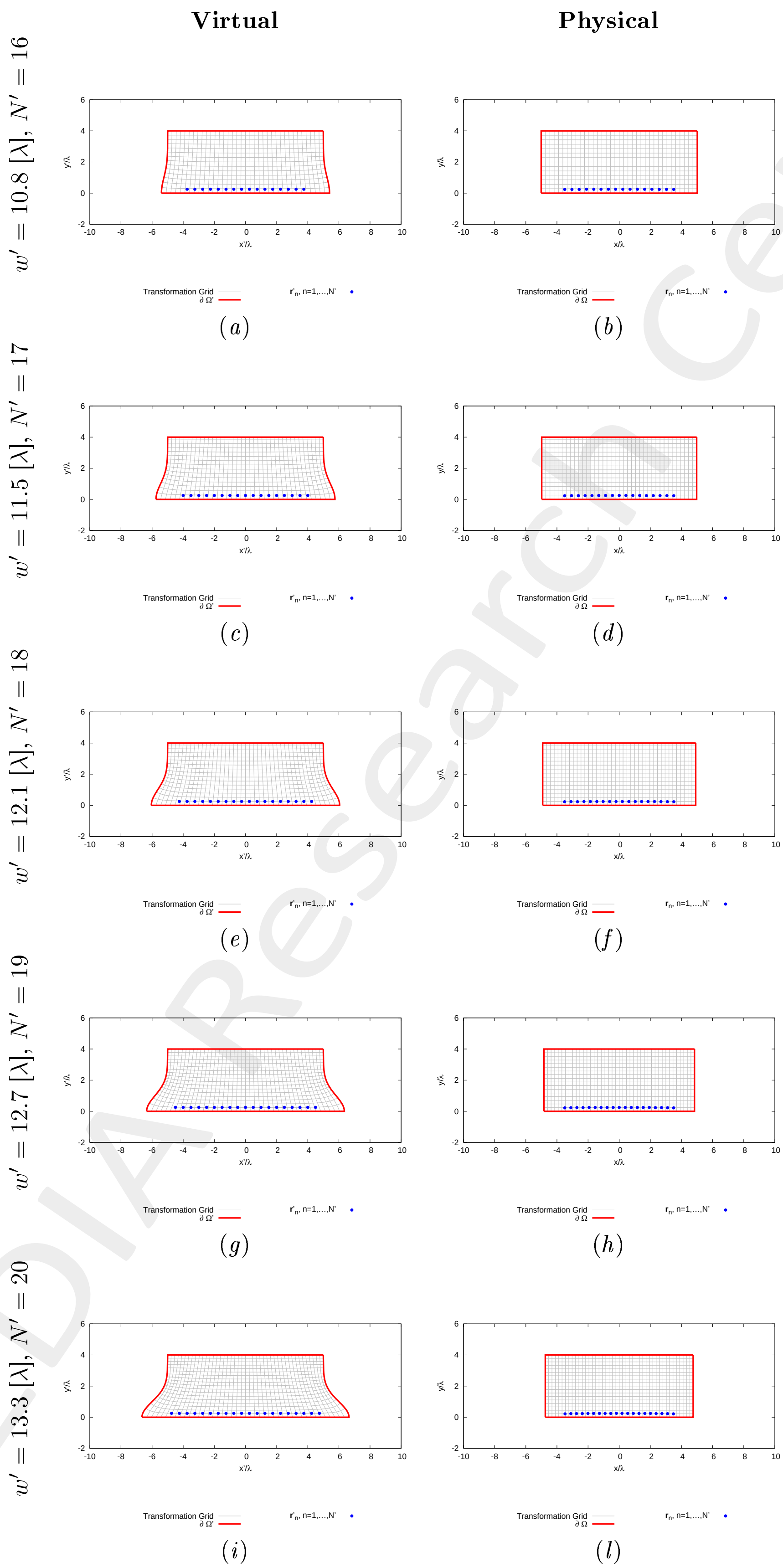

Figure 3: Transformation grids for different values of w'. Physical geometry has been shifted on y by $h/2 = 2.0$ [λ].

Lens Permittivity - $w' = 10.8$ $[\lambda]$

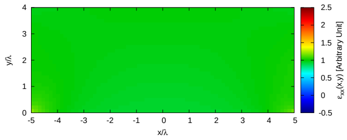

(a) ε_{xx}

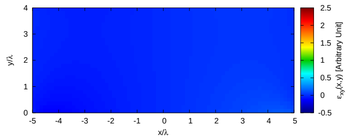

(b) ε_{xy}

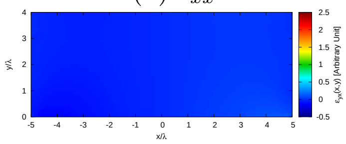

(c) ε_{yx}

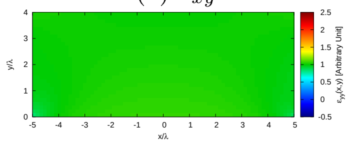

(d) ε_{yy}

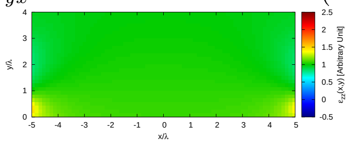

(e) ε_{zz}

Figure 4: Components of the relative permittivity tensor of the lens.

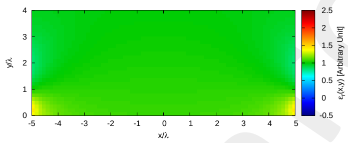

Figure 5: Isotropic approximate permittivity distribution of the lens.

Lens Permittivity - $w' = 11.5$ $[\lambda]$

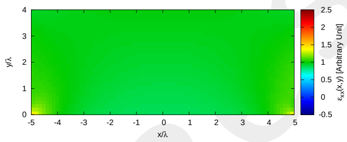

(a) ε_{xx}

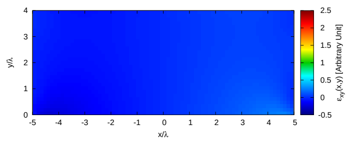

(b) ε_{xy}

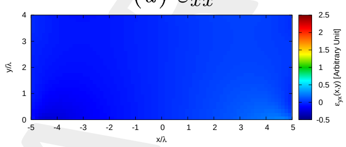

(c) ε_{yx}

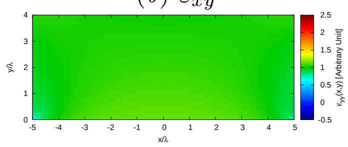

(d) ε_{yy}

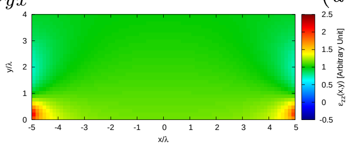

(e) ε_{zz}

Figure 6: Components of the relative permittivity tensor of the lens.

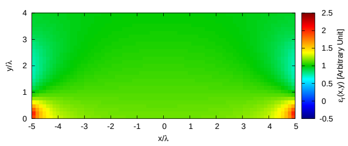

Figure 7: Isotropic approximate permittivity distribution of the lens.

Lens Permittivity - $w' = 12.1$ $[\lambda]$

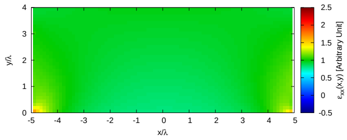

(a) ε_{xx}

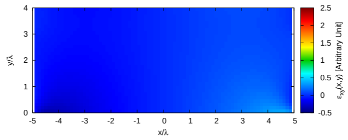

(b) ε_{xy}

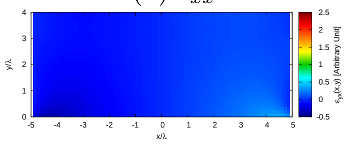

(c) ε_{yx}

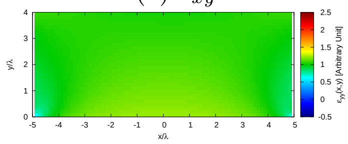

(d) ε_{yy}

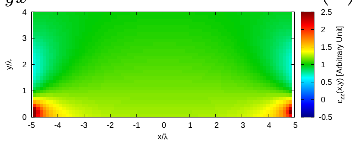

(e) ε_{zz}

Figure 8: Components of the relative permittivity tensor of the lens.

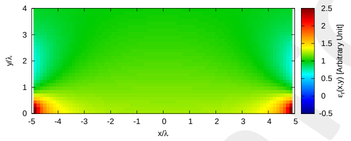

Figure 9: Isotropic approximate permittivity distribution of the lens.

Lens Permittivity - $w' = 12.7$ $[\lambda]$

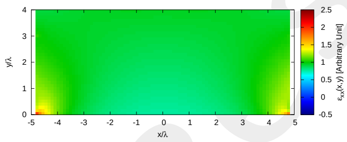

(a) ε_{xx}

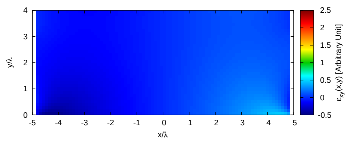

(b) ε_{xy}

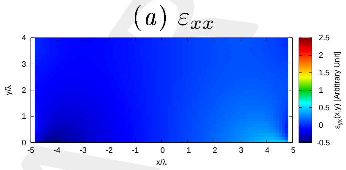

(c) ε_{yx}

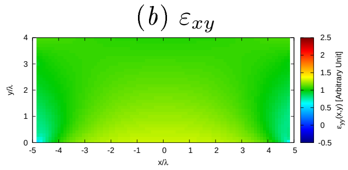

(d) ε_{yy}

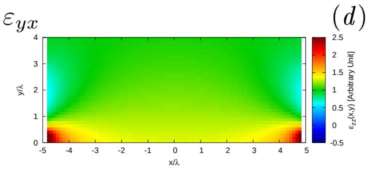

(e) ε_{zz}

Figure 10: Components of the relative permittivity tensor of the lens.

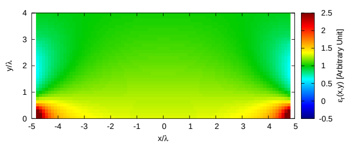

Figure 11: Isotropic approximate permittivity distribution of the lens.

Lens Permittivity - $w' = 13.3$ [λ]

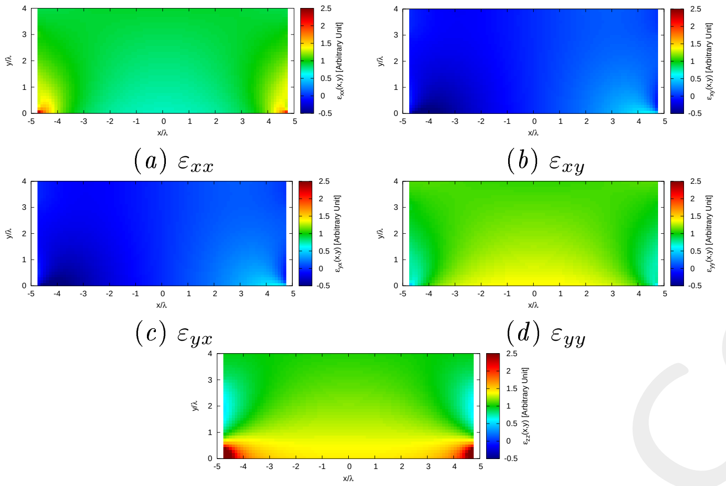

(a) ε_{xx} (b) ε_{xy} (c) ε_{yx} (d) ε_{yy} (e) ε_{zz}

Figure 12: Components of the relative permittivity tensor of the lens.

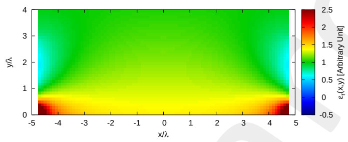

Figure 13: Isotropic approximate permittivity distribution of the lens.

Physical Lens Parameters

Parameter	$w' = 10.8$ [λ]	$w' = 11.5$ [λ]	$w' = 12.1$ [λ]	$w' = 12.7$ [λ]	$w' = 13.3$ [λ]
Height, h [λ]	4.00	4.00	4.00	4.00	4.00
Width, w [λ]	10.03	9.95	9.83	9.68	9.50
Anisotropic Permittivity Range	$[-0.12, 1.46]$	$[-0.24, 2.08]$	$[-0.35, 2.78]$	$[-0.46, 3.64]$	$[-0.58, 4.61]$
Isotropic Permittivity Range	$[0.00, 1.44]$	$[0.00, 2.00]$	$[0.00, 2.62]$	$[0.00, 3.37]$	$[0.00, 4.34]$
Average Fractional Anisotropy, α_F	5.39×10^{-2}	1.03×10^{-1}	1.44×10^{-1}	1.84×10^{-1}	2.23×10^{-1}
Average Relative Anisotropy, α_R	4.45×10^{-2}	8.86×10^{-2}	1.22×10^{-1}	1.59×10^{-1}	1.96×10^{-1}

Table III: Transformation statistics. Note that we impose $h = h'$, while w is internally chosen by the QCTO software.

Virtual Grid Orthogonality

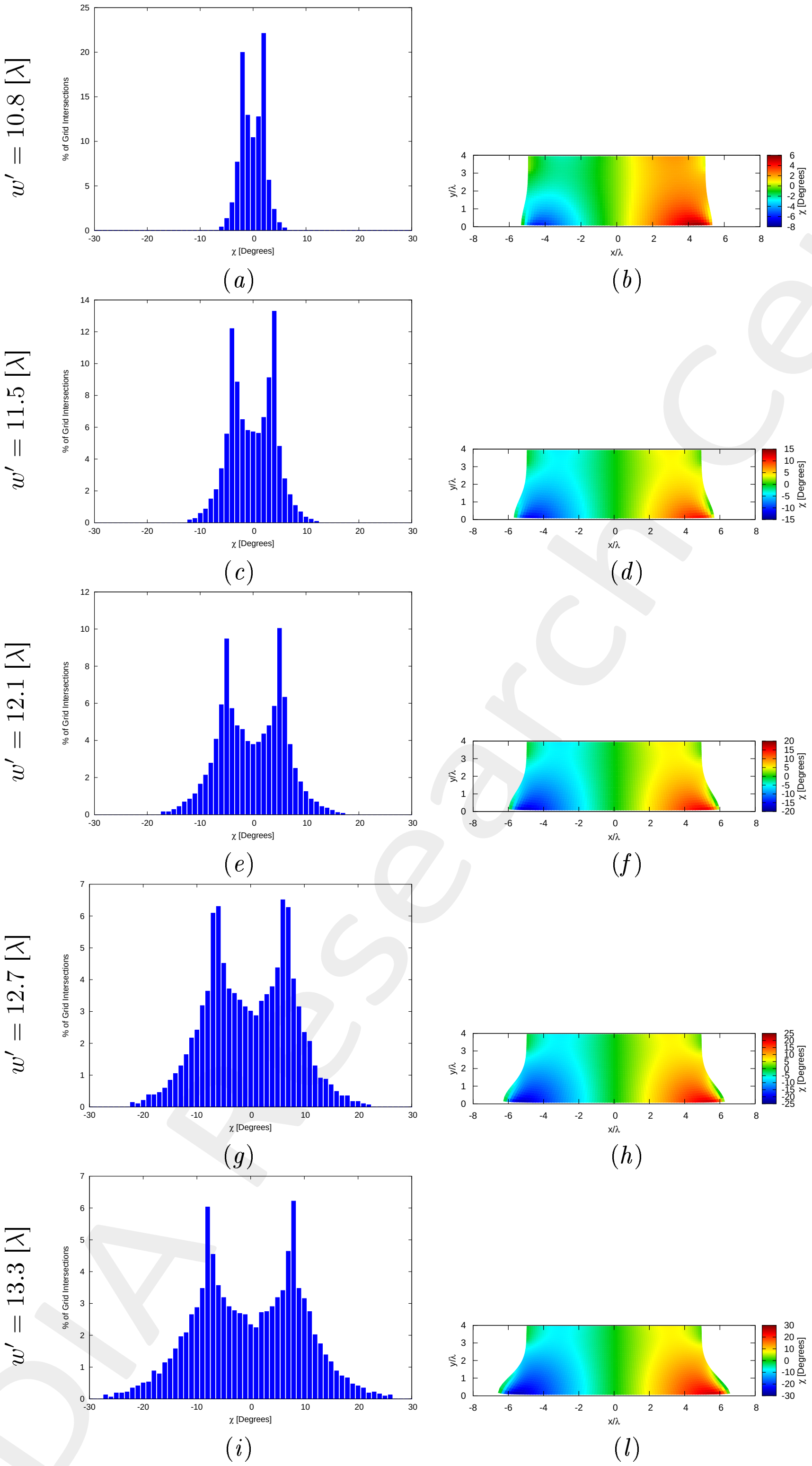

Figure 14: Orthogonality of the virtual grid for different values of w'.

1.2.2 Near-Field Distributions ($\phi_s = 90$ [deg], $f = 600$ [MHz])

Case $w' = 10.8$ $[\lambda]$, $N' = 16$

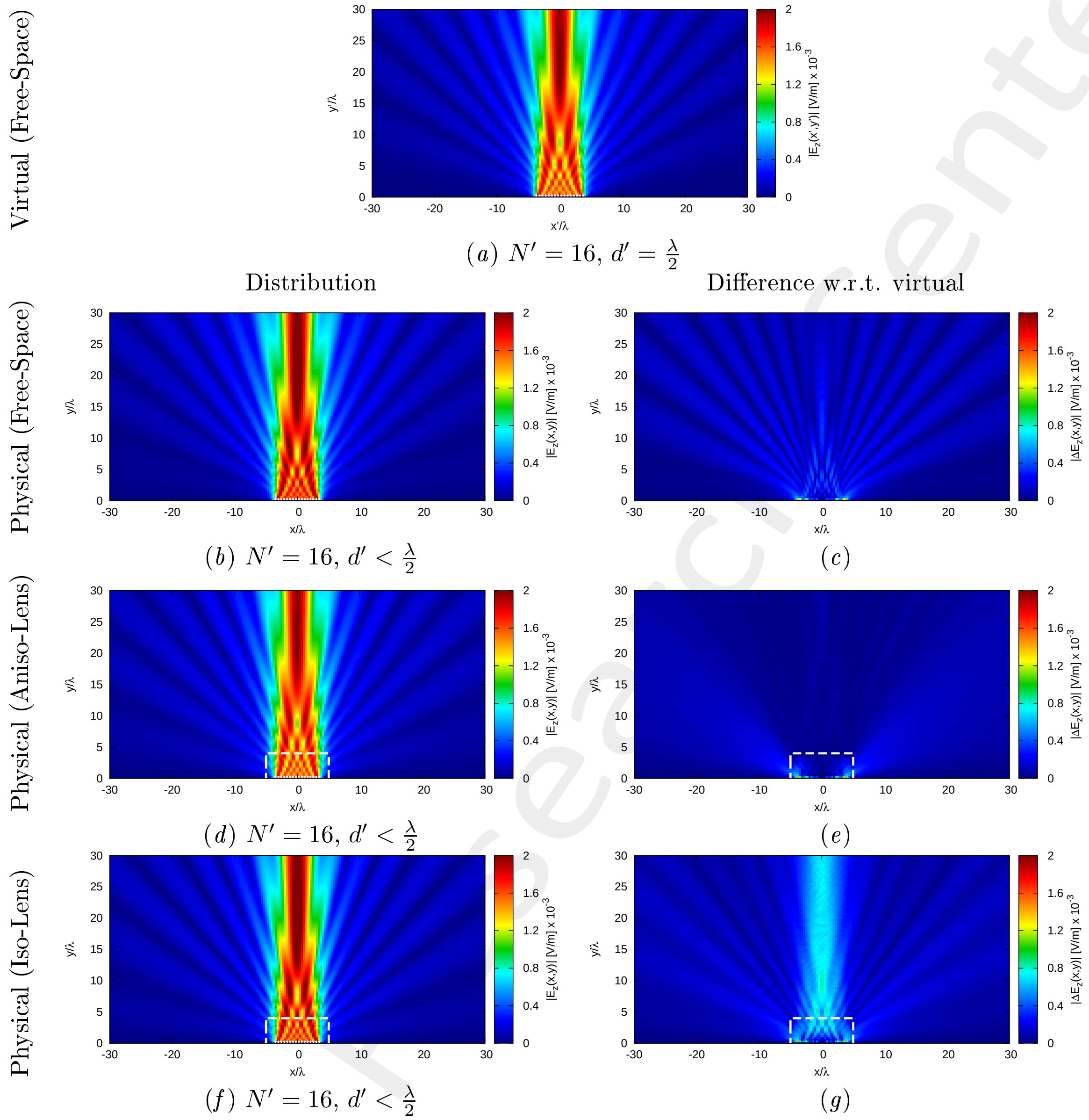

Figure 15: Electric field distributions.

Case $w' = 11.5$ **[**λ**],** $N' = 17$

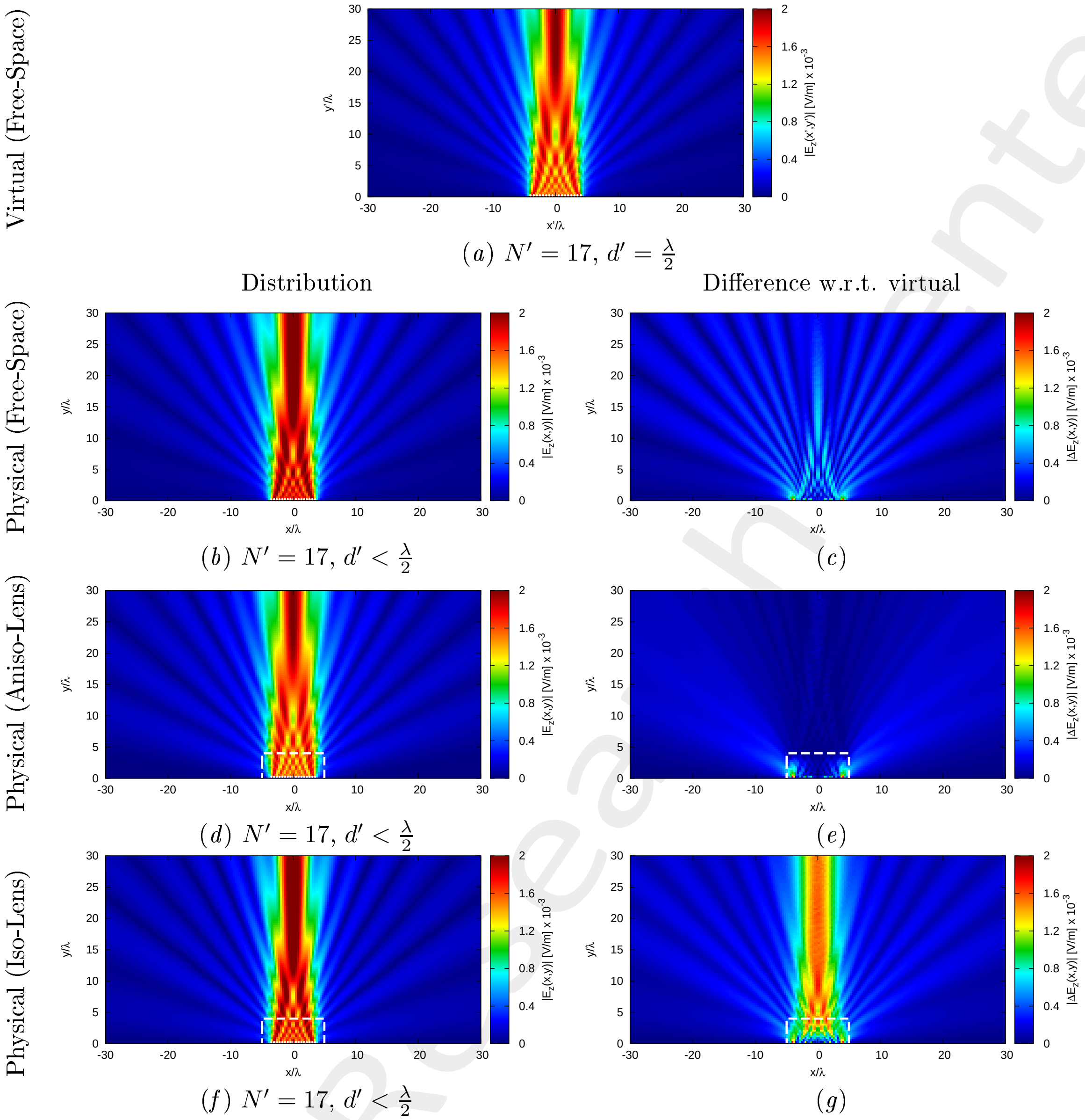

(a) $N' = 17$, $d' = \frac{\lambda}{2}$

(b) $N' = 17$, $d' < \frac{\lambda}{2}$ (c)

(d) $N' = 17$, $d' < \frac{\lambda}{2}$ (e)

(f) $N' = 17$, $d' < \frac{\lambda}{2}$ (g)

Figure 16: Electric field distributions.

Case $w' = 12.1$ **[**λ**],** $N' = 18$

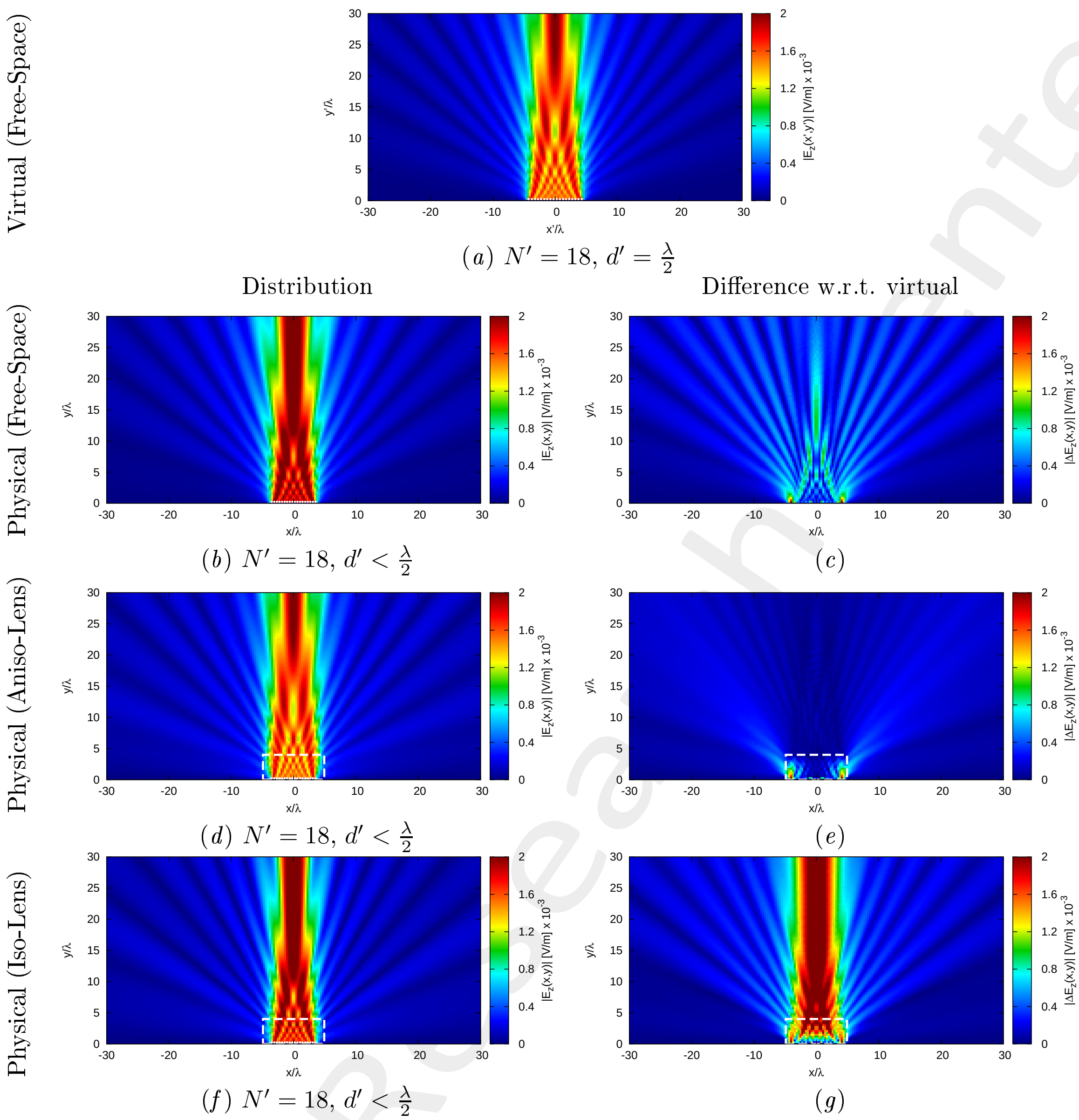

Figure 17: Electric field distributions.

Case $w' = 12.7$ **[**λ**]**, $N' = 19$

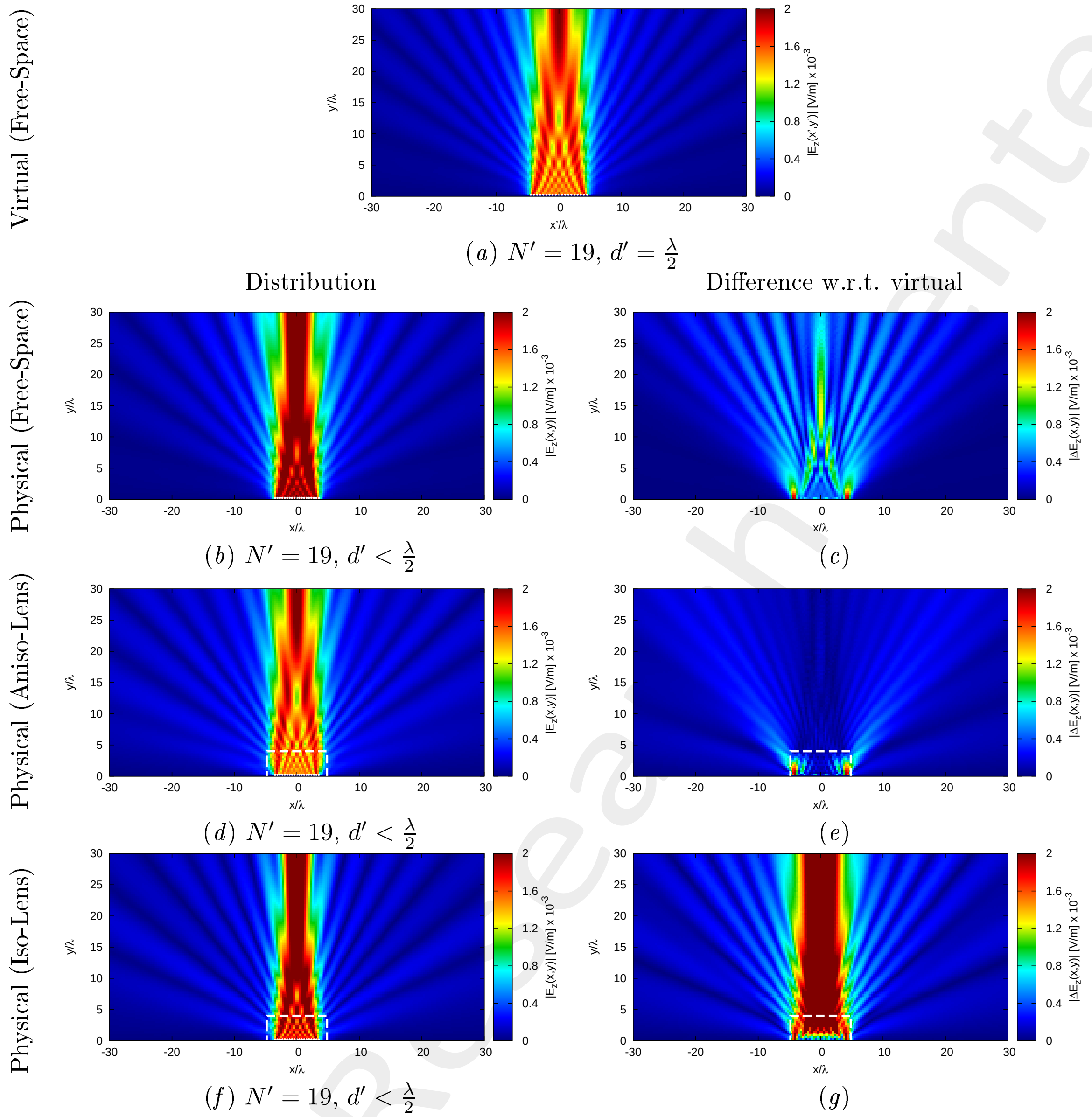

Figure 18: Electric field distributions.

Case $w' = 13.3$ [λ], $N' = 20$

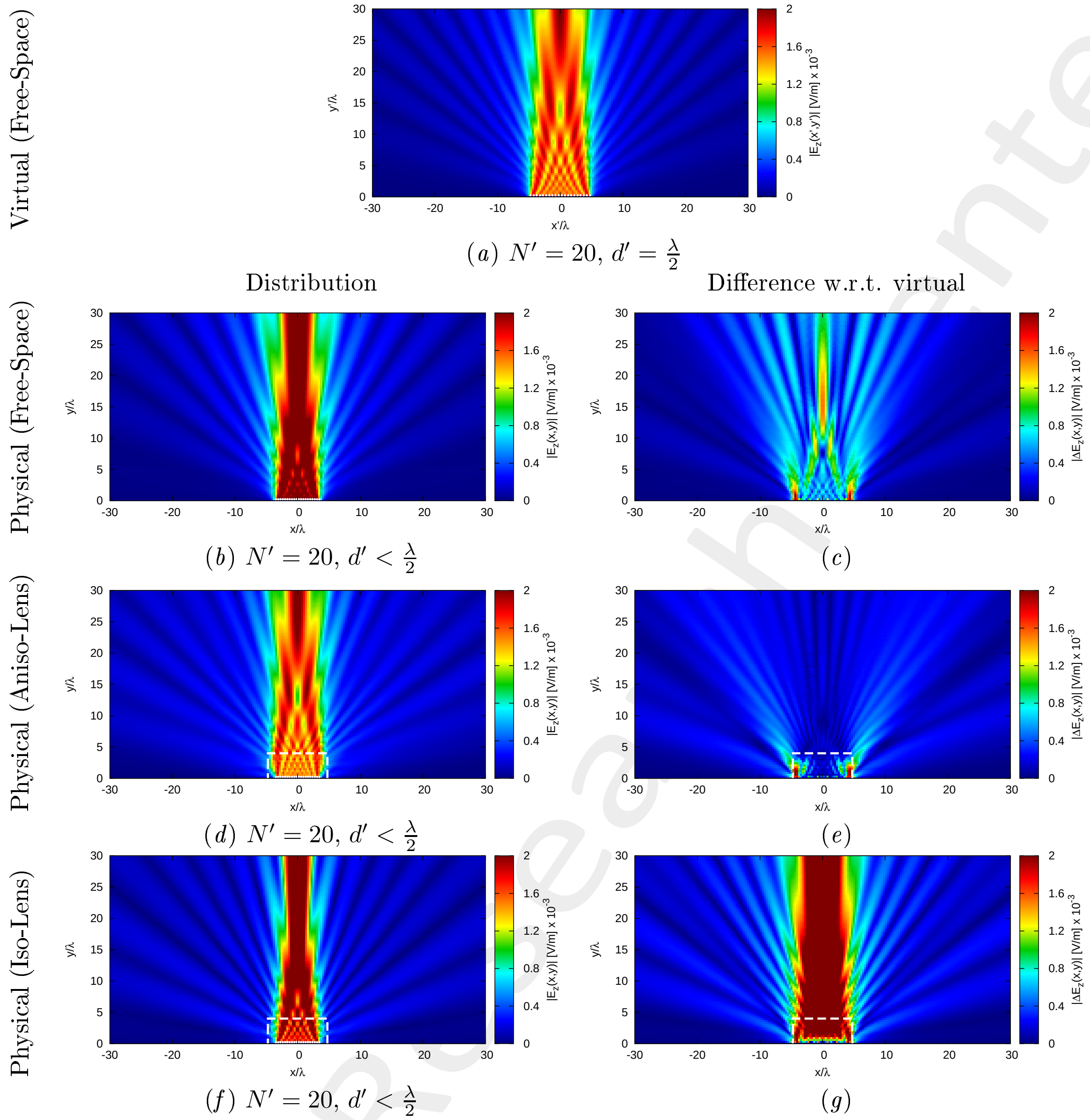

(a) $N' = 20$, $d' = \frac{\lambda}{2}$

(b) $N' = 20$, $d' < \frac{\lambda}{2}$ (c)

(d) $N' = 20$, $d' < \frac{\lambda}{2}$ (e)

(f) $N' = 20$, $d' < \frac{\lambda}{2}$ (g)

Figure 19: Electric field distributions.

1.2.3 Far-Field Patterns ($\phi_s = 90$ [deg], $f = 600$ [MHz])

Anisotropic Lens

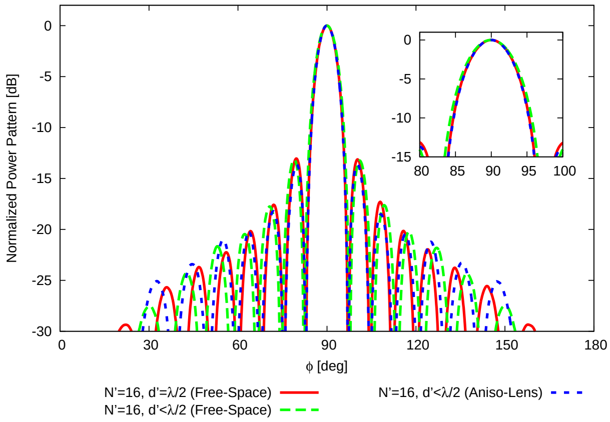

(a) $w' = 10.8$ [λ], $N' = 16$

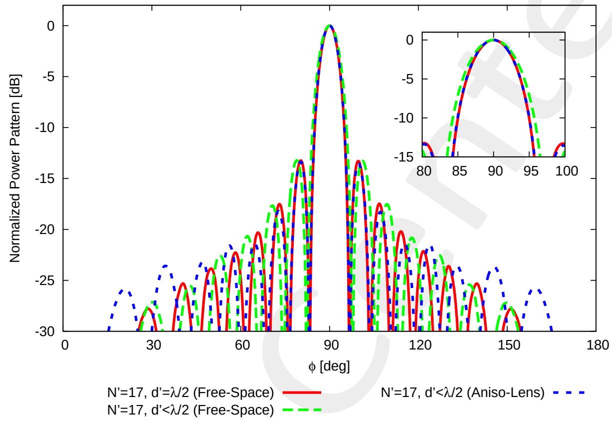

(b) $w' = 11.5$ [λ], $N' = 17$

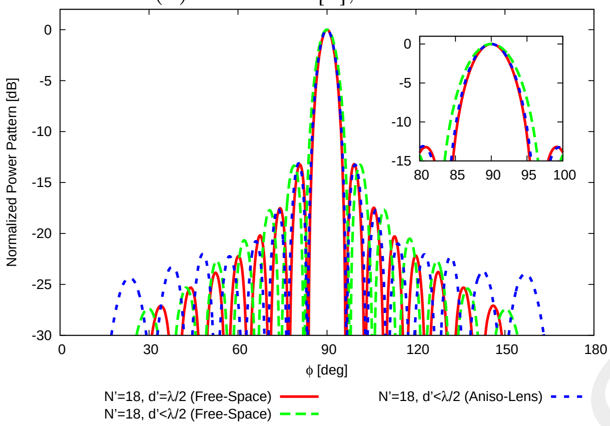

(c) $w' = 12.1$ [λ], $N' = 18$

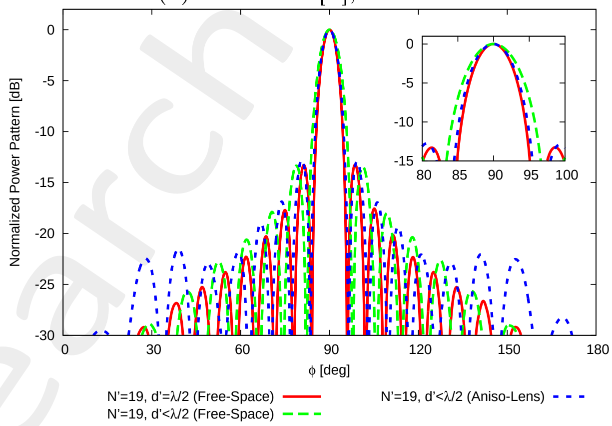

(d) $w' = 12.7$ [λ], $N' = 19$

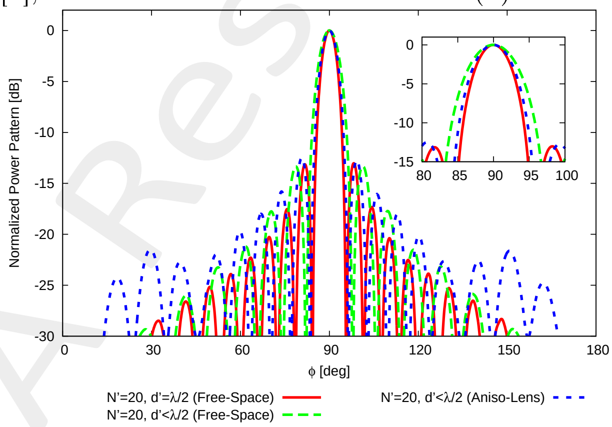

(e) $w' = 13.3$ [λ], $N' = 20$

Figure 20: Far field pattern comparison for different values of w'.

Isotropic Lens

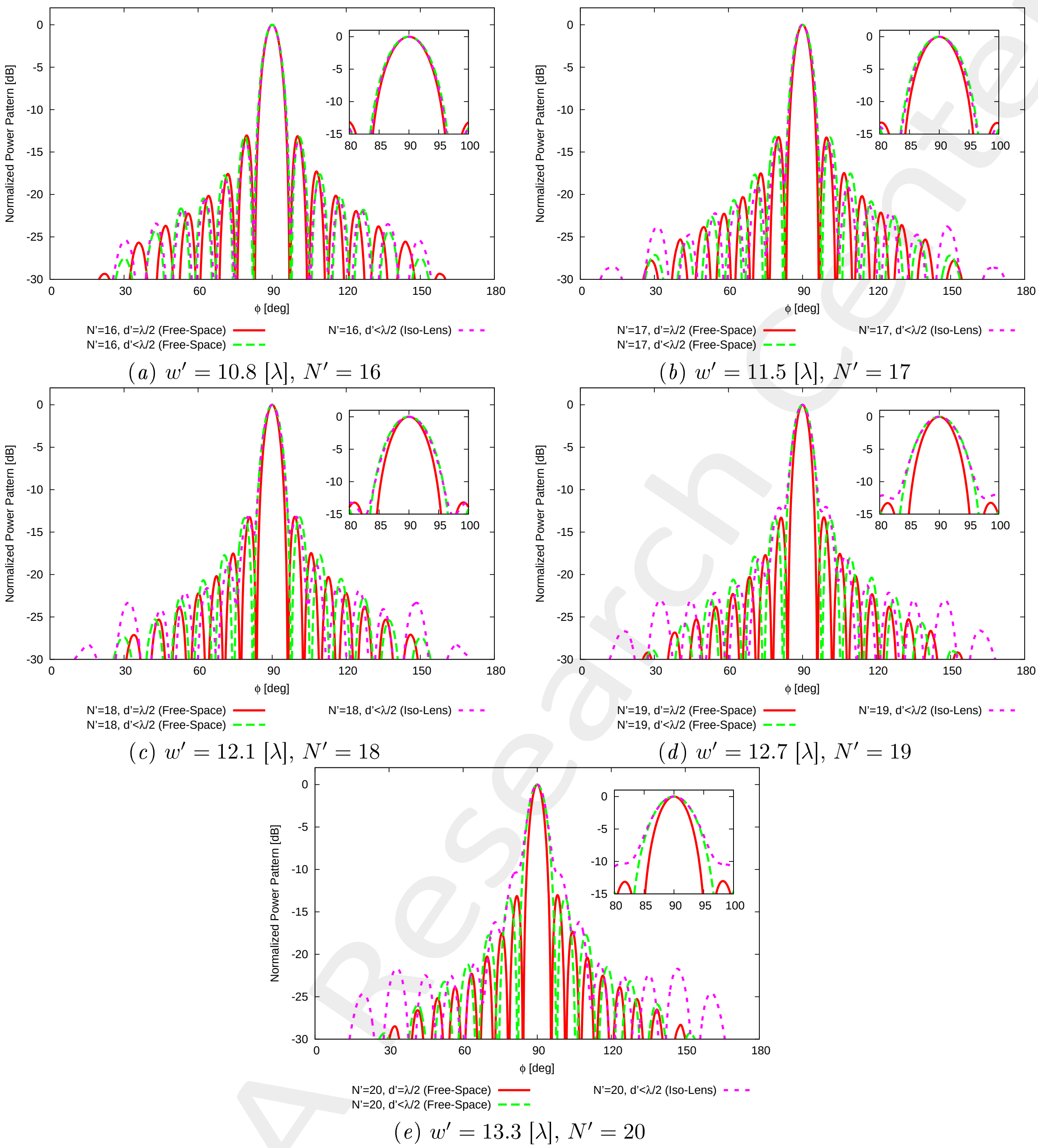

Figure 21: Far field pattern comparison for different values of w'.

1.2.4 Summary ($\phi_s = 90$ [deg], $f = 600$ [MHz])

$w' = 10.8$ [λ]				
	Virtual Array	**Physical Array**		
Environment	Free-Space	Free-Space	Aniso-Lens	Iso-Lens
Number of elements	16	16		
Spacing [λ]	0.5	< 0.5		
Aperture [λ]	7.5	7.00		
$D_{\max}$ [dB]	13.97	13.71	14.03	13.87
SLL [dB]	13.11	13.17	13.63	13.82
$FNBW$ [deg]	14.32	15.40	14.32	14.95
$3dB$ Beamwidth [deg]	6.36	6.79	6.28	6.53
Matching Error, ξ (w.r.t. virtual, outside lens)	-	3.50×10^{-1}	2.48×10^{-1}	5.62×10^{-1}

$w' = 11.5$ [λ]				
	Virtual Array	**Physical Array**		
Environment	Free-Space	Free-Space	Aniso-Lens	Iso-Lens
Number of elements	17	17		
Spacing [λ]	0.5	< 0.5		
Aperture [λ]	8.0	7.00		
$D_{\max}$ [dB]	14.25	13.69	14.21	13.88
SLL [dB]	13.16	13.23	13.37	13.76
$FNBW$ [deg]	13.60	15.40	13.60	14.86
$3dB$ Beamwidth [deg]	5.97	6.84	5.99	6.44
Matching Error, ξ (w.r.t. virtual, outside lens)	-	5.94×10^{-1}	3.67×10^{-1}	9.63×10^{-1}

$w' = 12.1$ [λ]				
	Virtual Array	**Physical Array**		
Environment	Free-Space	Free-Space	Aniso-Lens	Iso-Lens
Number of elements	18	18		
Spacing [λ]	0.5	< 0.5		
Aperture [λ]	8.5	7.02		
$D_{\max}$ [dB]	14.50	13.70	14.27	13.74
SLL [dB]	13.14	13.26	13.12	13.22
$FNBW$ [deg]	12.79	15.49	13.24	15.04
$3dB$ Beamwidth [deg]	5.64	6.84	5.84	6.52
Matching Error, ξ (w.r.t. virtual, outside lens)	-	7.04×10^{-1}	4.19×10^{-1}	1.20

$w' = 12.7$ [λ]				
	Virtual Array	**Physical Array**		
Environment	Free-Space	Free-Space	Aniso-Lens	Iso-Lens
Number of elements	19	19		
Spacing [λ]	0.5	< 0.5		
Aperture [λ]	9.0	6.99		
$D_{\max}$ [dB]	14.73	13.68	14.27	13.46
SLL [dB]	13.06	13.36	12.76	12.03
$FNBW$ [deg]	12.07	15.67	12.97	15.49
$3dB$ Beamwidth [deg]	5.35	6.89	5.75	6.73
Matching Error, ξ (w.r.t. virtual, outside lens)	-	6.96×10^{-1}	4.63×10^{-1}	1.44

$w' = 13.3$ [λ]				
	Virtual Array	**Physical Array**		
Environment	Free-Space	Free-Space	Aniso-Lens	Iso-Lens
Number of elements	20	20		
Spacing [λ]	0.5	< 0.5		
Aperture [λ]	9.5	6.96		
$D_{\max}$ [dB]	14.96	13.63	14.21	13.03
SLL [dB]	13.18	13.32	12.49	16.18
$FNBW$ [deg]	11.44	15.76	12.88	28.90
$3dB$ Beamwidth [deg]	5.06	6.97	5.72	7.04
Matching Error, ξ (w.r.t. virtual, outside lens)	-	7.31×10^{-1}	5.67×10^{-1}	1.63

Table IV: Summary for step 2.

1.3 Source Inversion (SI)

Parameters

- Before SI
  - Number of elements: $N' = \{16; 17; 18; 19; 20\}$, $d' < \lambda/2$;
- After SI
  - Number of elements after SI: $N = 15$, $d = \frac{\lambda}{2}$;
  - Aperture: $L = 7.0$;
- Radius of the observation domain: $r_{SI} = 50.0$ $[\lambda]$;
- Number of field sampling points: $n_{SI} = 1000$.

1.3.1 Results of the SI ($\phi_s = 90$ [deg], $f = 600$ [MHz])

Synthesized Excitations

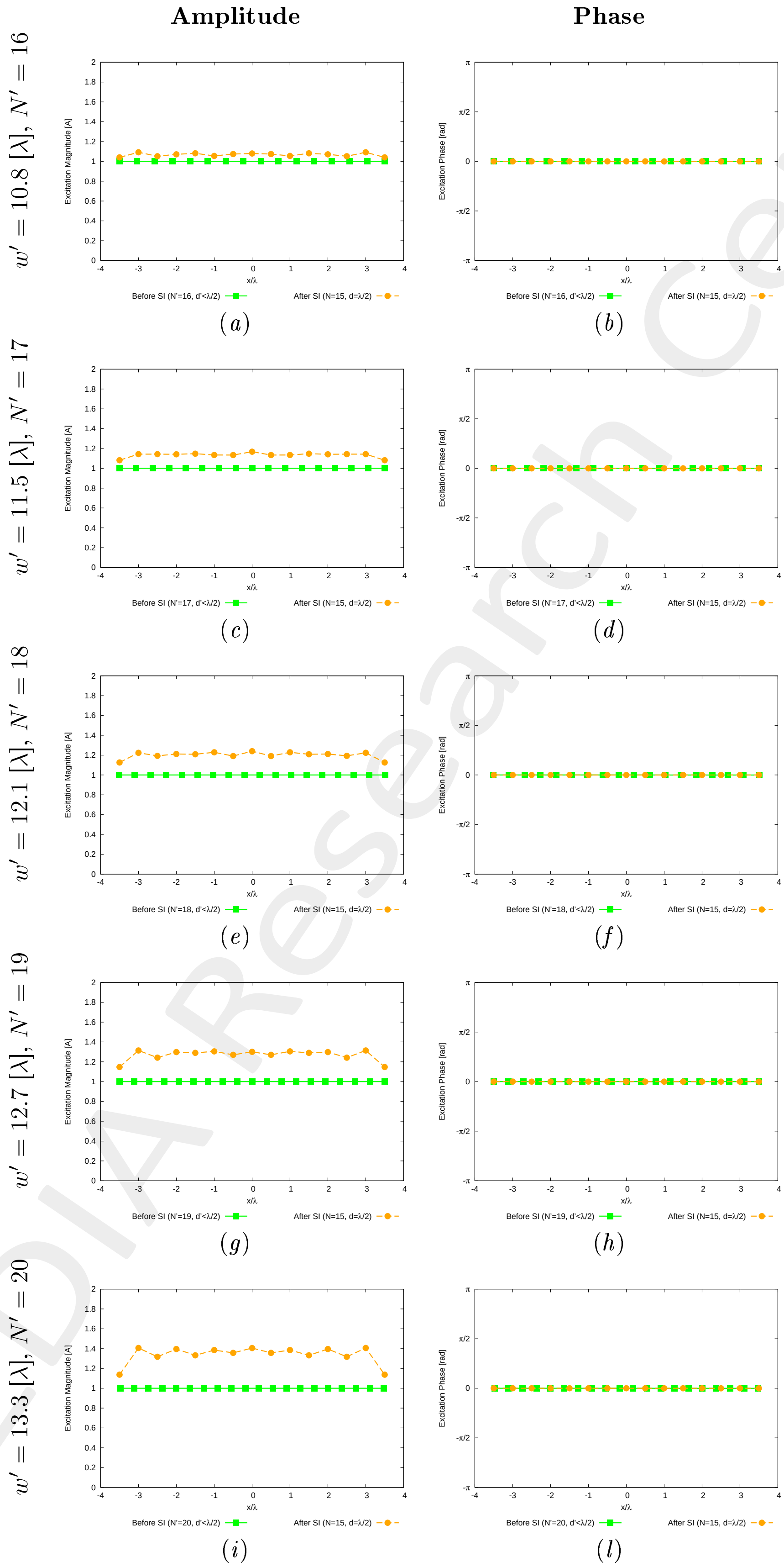

Figure 22: $\phi_s = 90$ [deg], $f = 600$ [MHz] - Synthesized excitations through SI.

Check SI: Free-Space Patterns

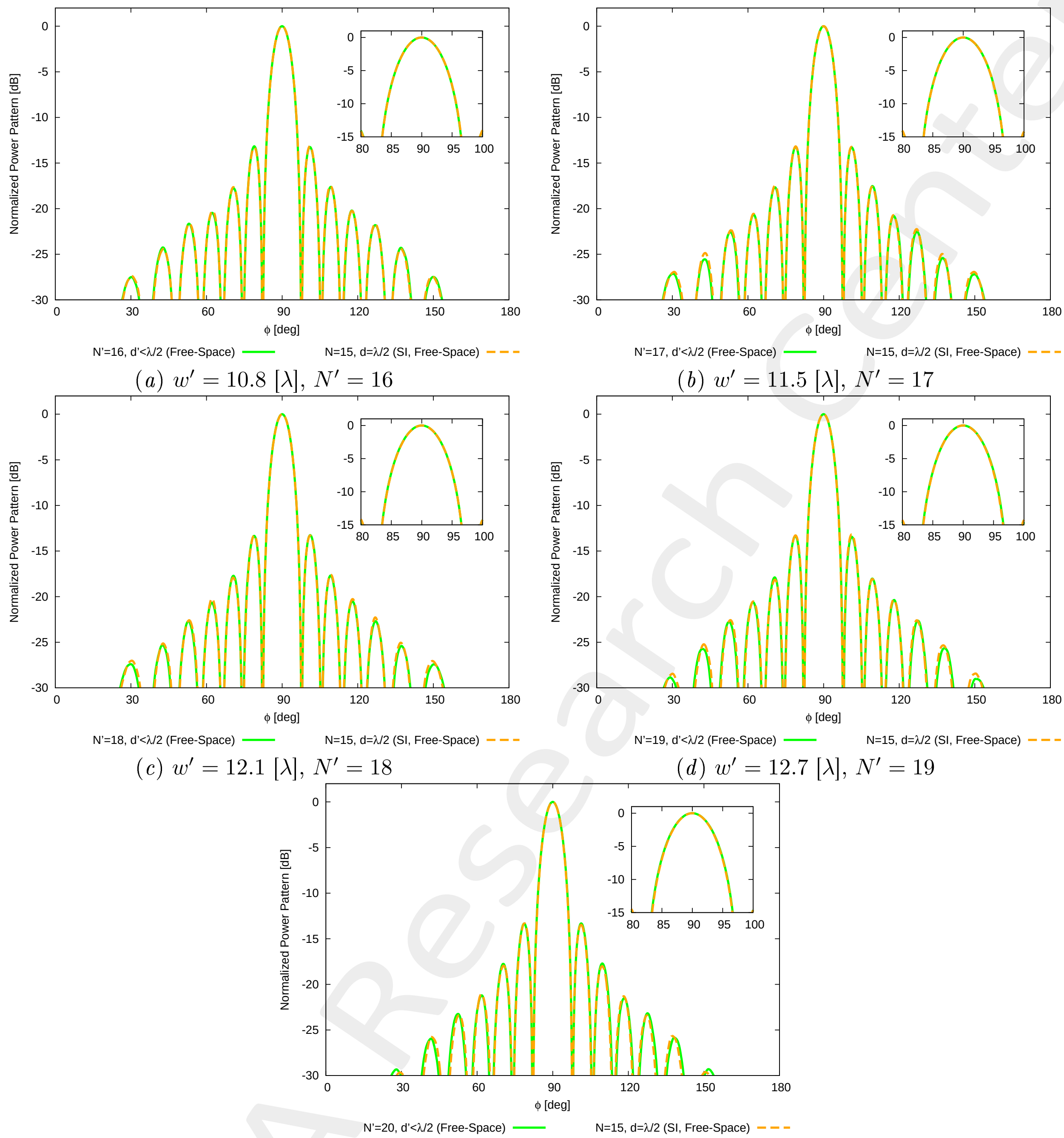

(a) $w' = 10.8$ $[\lambda]$, $N' = 16$ (b) $w' = 11.5$ $[\lambda]$, $N' = 17$

(c) $w' = 12.1$ $[\lambda]$, $N' = 18$ (d) $w' = 12.7$ $[\lambda]$, $N' = 19$

(e) $w' = 13.3$ $[\lambda]$, $N' = 20$

Figure 23: $\phi_s = 90$ [deg], $f = 600$ [MHz] - Free-space far field pattern comparison for different values of w'.

1.3.2 Near-Field Distribution ($\phi_s = 90$ [deg], $f = 600$ [MHz])

Case $w' = 10.8$ [λ], $N' = 16$

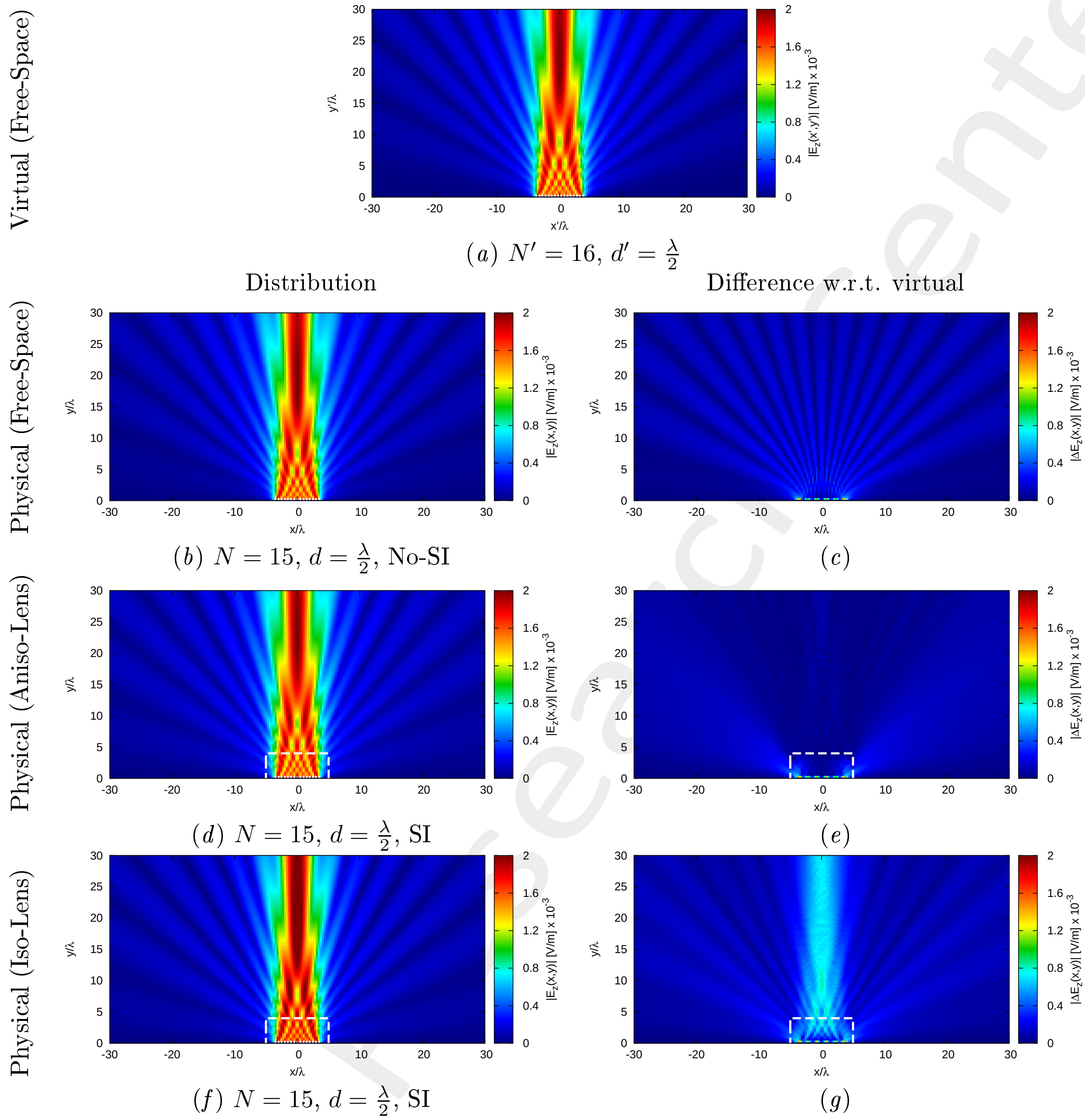

Figure 24: $\phi_s = 90$ [deg], $f = 600$ [MHz] - Electric field distributions.

Case $w' = 11.5$ **[**λ**],** $N' = 17$

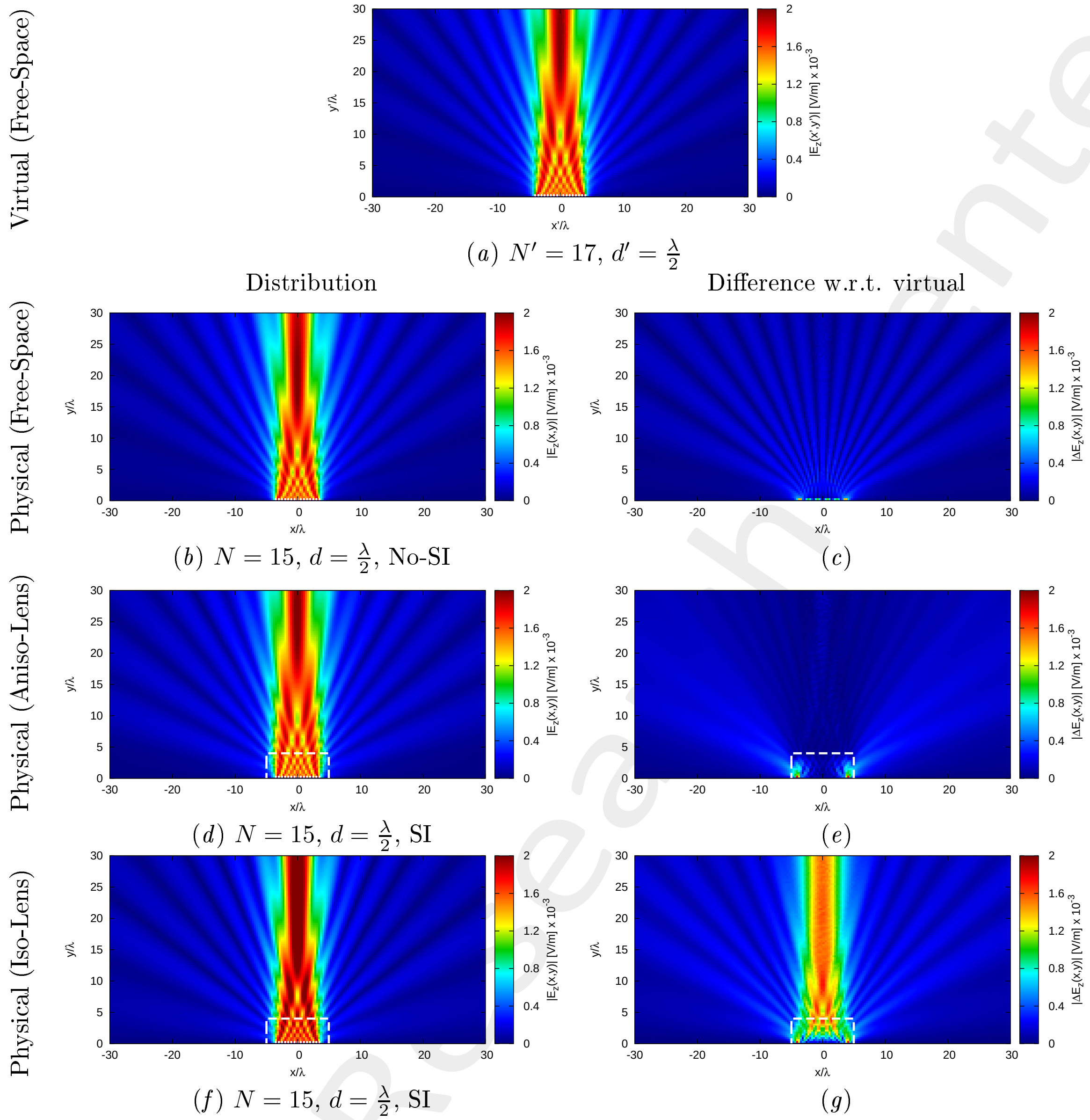

Figure 25: $\phi_s = 90$ [deg], $f = 600$ [MHz] - Electric field distributions.

Case $w' = 12.1$ **[**λ**],** $N' = 18$

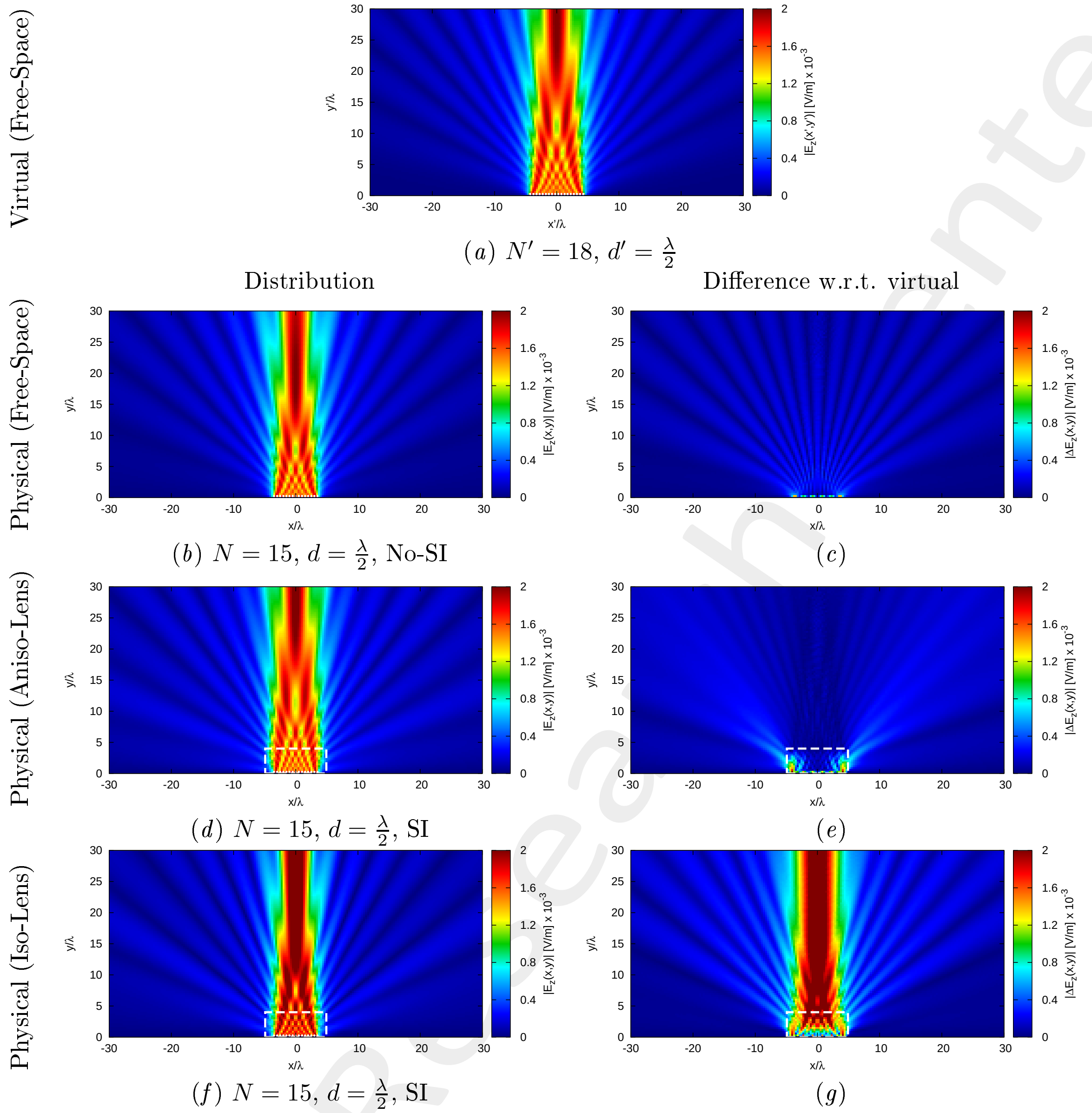

Figure 26: $\phi_s = 90$ [deg], $f = 600$ [MHz] - Electric field distributions.

Case $w' = 12.7$ [λ], $N' = 19$

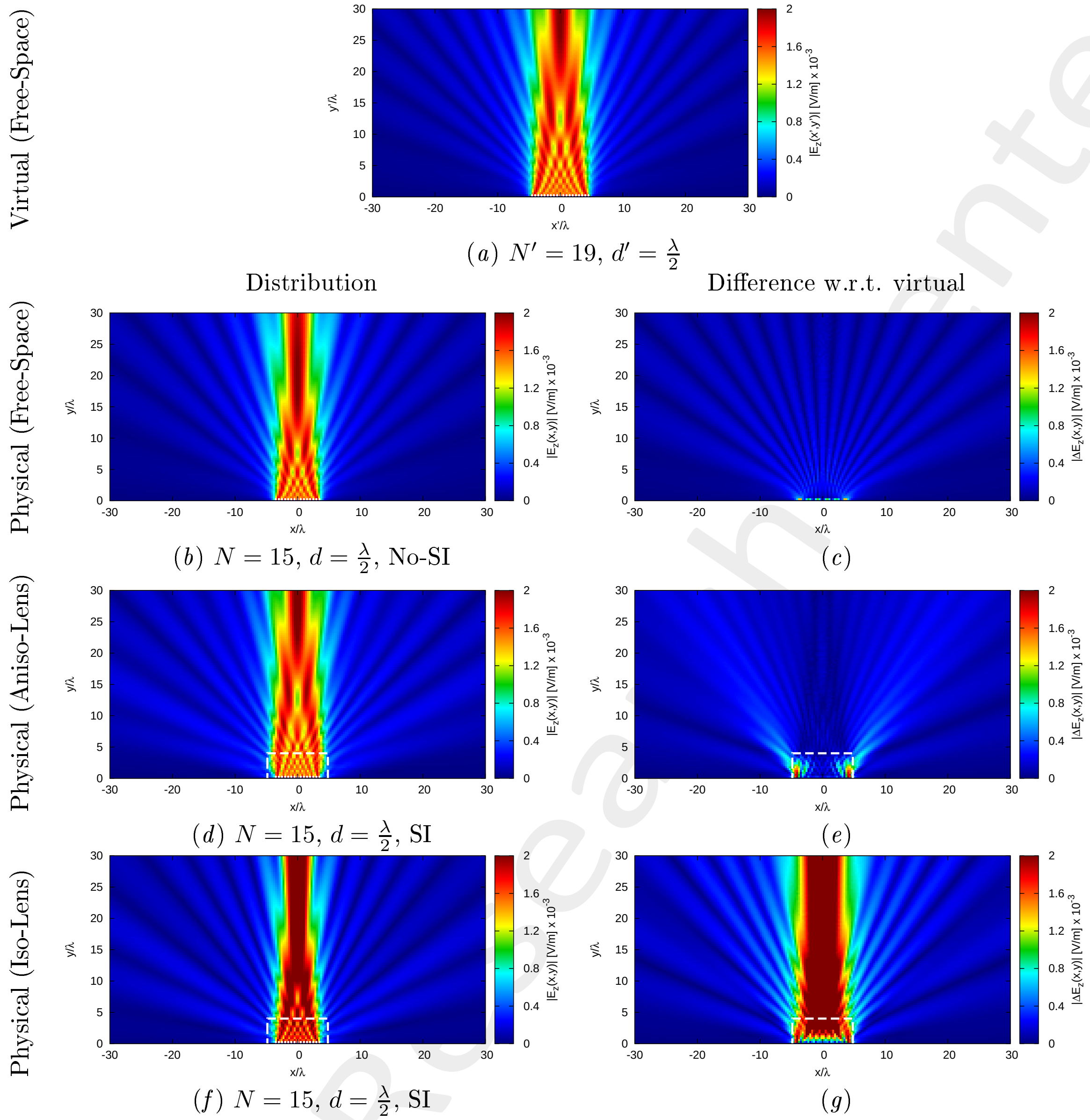

Figure 27: $\phi_s = 90$ [deg], $f = 600$ [MHz] - Electric field distributions.

Case $w' = 13.3$ **[**λ**]**, $N' = 20$

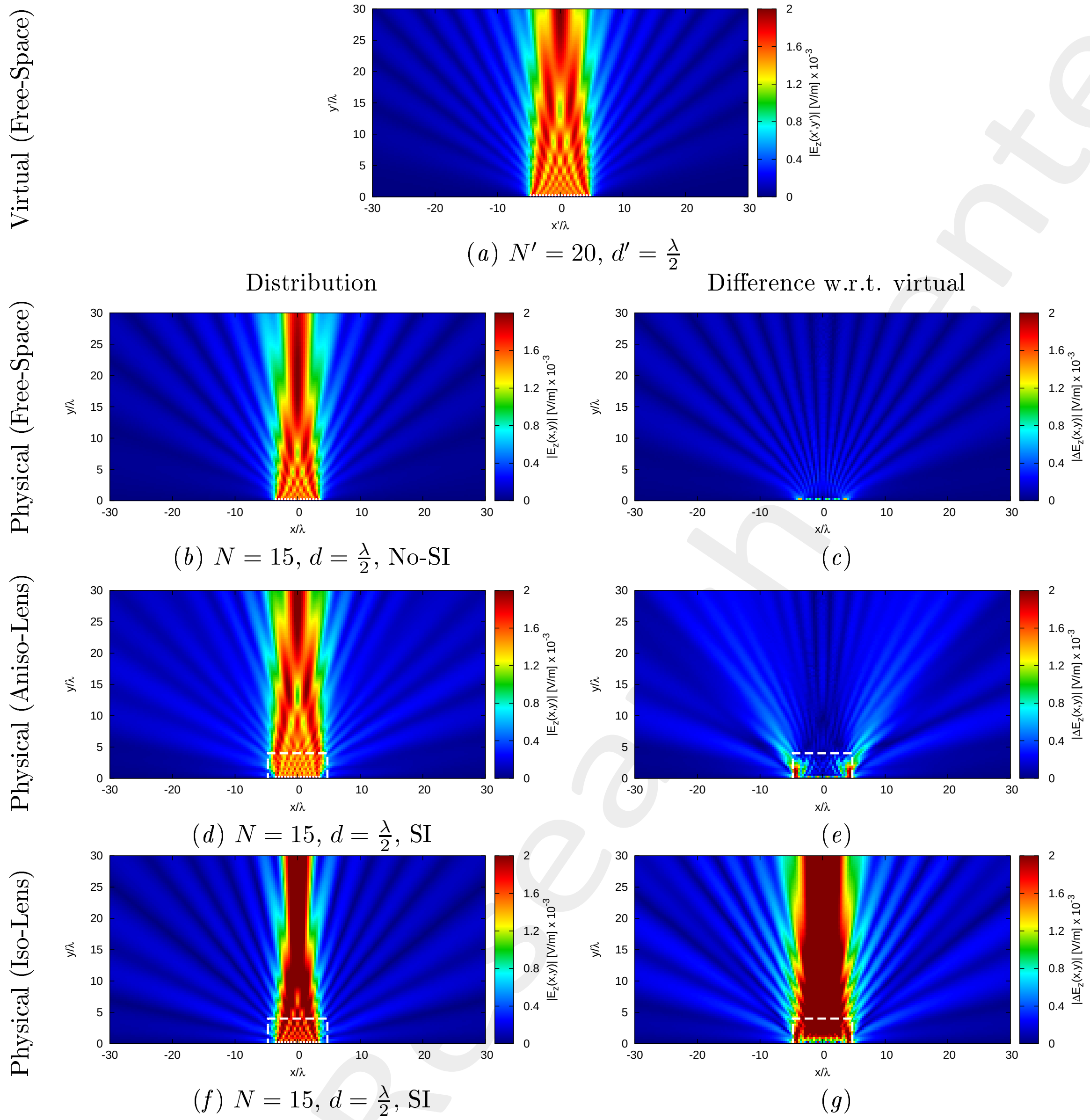

Figure 28: $\phi_s = 90$ [deg], $f = 600$ [MHz] - Electric field distributions.

1.3.3 Far-Field Patterns ($\phi_s = 90$ [deg], $f = 600$ [MHz])

Anisotropic Lens

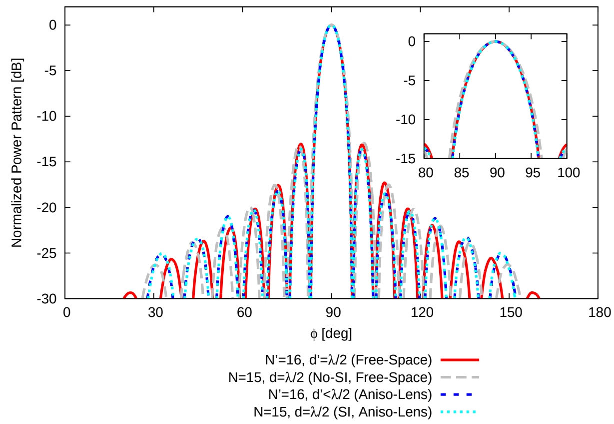

(a) $w' = 10.8$ [λ], $N' = 16$

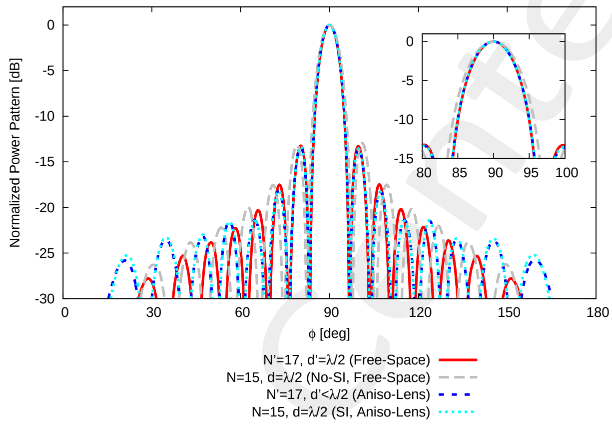

(b) $w' = 11.5$ [λ], $N' = 17$

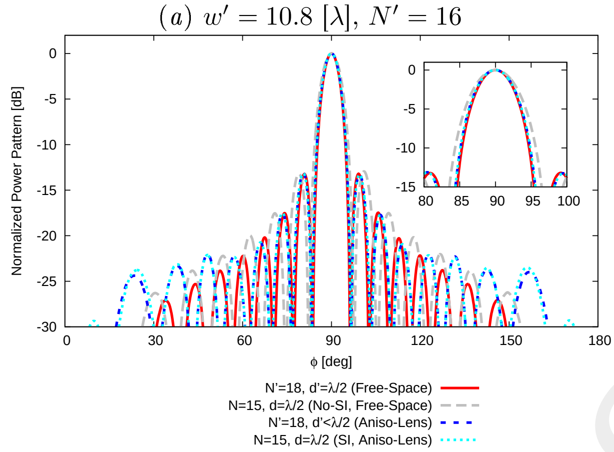

(c) $w' = 12.1$ [λ], $N' = 18$

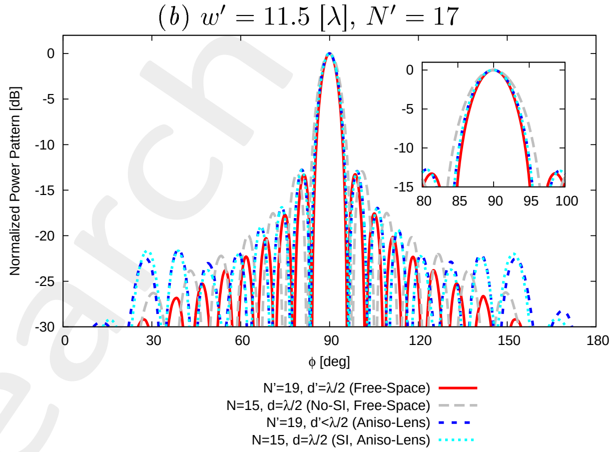

(d) $w' = 12.7$ [λ], $N' = 19$

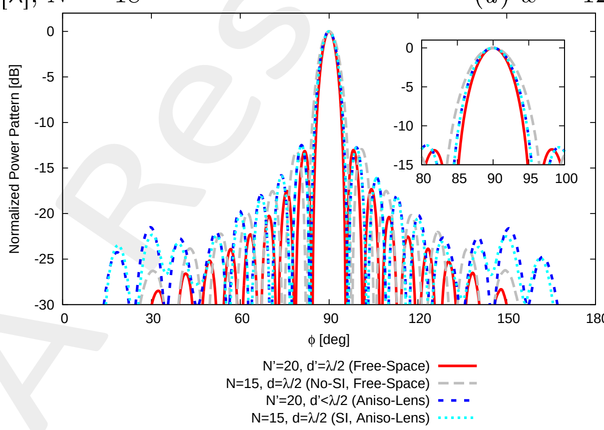

(e) $w' = 13.3$ [λ], $N' = 20$

Figure 29: $\phi_s = 90$ [deg], $f = 600$ [MHz] - Far field pattern comparison for different values of w'.

Isotropic Lens

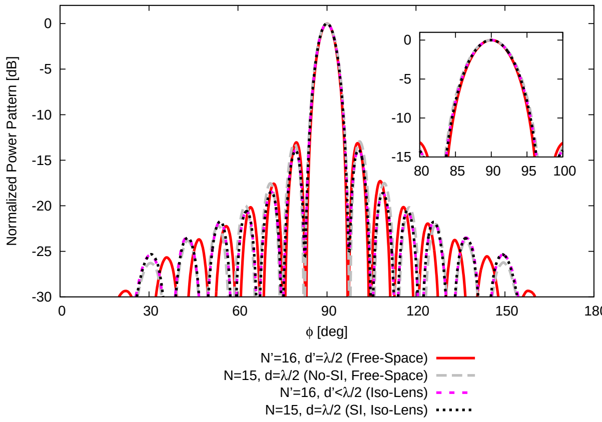

(a) $w' = 10.8$ [λ], $N' = 16$

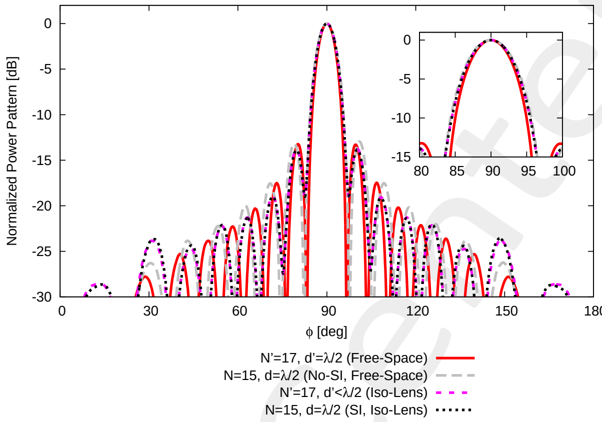

(b) $w' = 11.5$ [λ], $N' = 17$

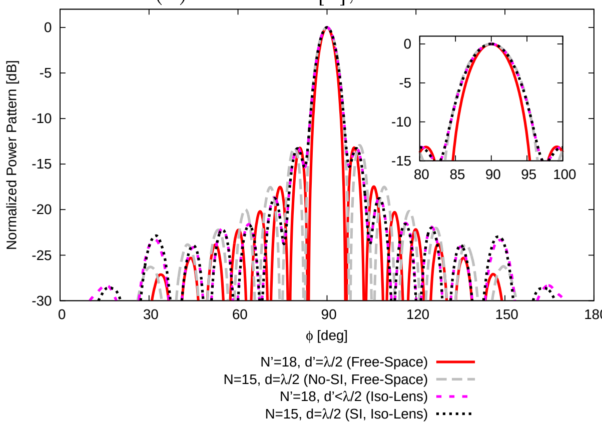

(c) $w' = 12.1$ [λ], $N' = 18$

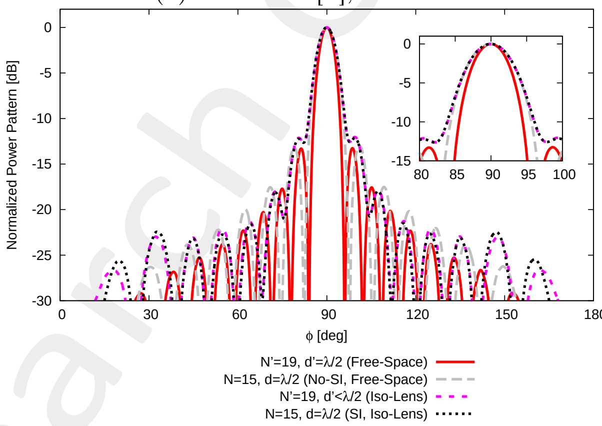

(d) $w' = 12.7$ [λ], $N' = 19$

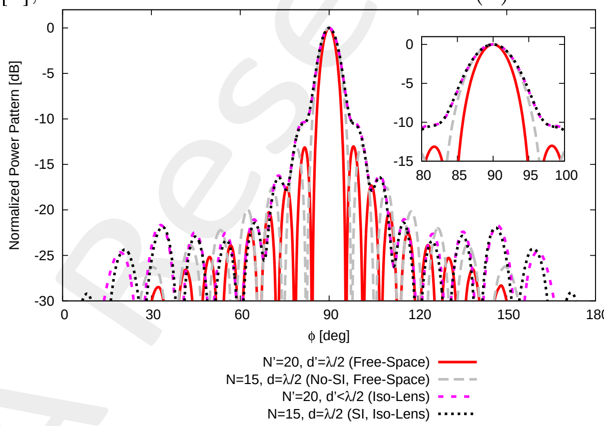

(e) $w' = 13.3$ [λ], $N' = 20$

Figure 30: $\phi_s = 90$ [deg], $f = 600$ [MHz] - Far field pattern comparison for different values of w'.

1.3.4 Final Summary ($\phi_s = 90$ [deg], $f = 600$ [MHz])

$w' = 10.8$ [λ]				
	Virtual Array	**Physical Array**		
Environment	Free-Space	Free-Space (No-SI)	Aniso-Lens (SI)	Iso-Lens (SI)
Number of elements	16	15		
Spacing [λ]	0.5	0.5		
Aperture [λ]	7.5	7.0		
$D_{\max}$ [dB]	13.97	13.71	14.03	13.87
SLL [dB]	13.11	13.08	13.62	13.85
$FNBW$ [deg]	14.32	15.31	14.32	14.95
$3dB$ Beamwidth [deg]	6.36	6.76	6.27	6.52
Matching Error, ξ (w.r.t. virtual, outside lens)	-	3.24×10^{-1}	2.45×10^{-1}	5.58×10^{-1}
$w' = 11.5$ [λ]				
	Virtual Array	**Physical Array**		
Environment	Free-Space	Free-Space (No-SI)	Aniso-Lens (SI)	Iso-Lens (SI)
Number of elements	17	15		
Spacing [λ]	0.5	0.5		
Aperture [λ]	8.0	7.0		
$D_{\max}$ [dB]	14.25	13.71	14.21	13.88
SLL [dB]	13.16	13.08	13.36	13.83
$FNBW$ [deg]	13.60	15.31	13.60	14.86
$3dB$ Beamwidth [deg]	5.97	6.76	5.99	6.45
Matching Error, ξ (w.r.t. virtual, outside lens)	-	5.57×10^{-1}	3.74×10^{-1}	9.62×10^{-1}
$w' = 12.1$ [λ]				
	Virtual Array	**Physical Array**		
Environment	Free-Space	Free-Space (No-SI)	Aniso-Lens (SI)	Iso-Lens (SI)
Number of elements	18	15		
Spacing [λ]	0.5	0.5		
Aperture [λ]	8.5	7.0		
$D_{\max}$ [dB]	14.50	13.71	14.26	13.73
SLL [dB]	13.14	13.08	13.13	13.28
$FNBW$ [deg]	12.79	15.31	13.24	15.04
$3dB$ Beamwidth [deg]	5.64	6.76	5.84	6.54
Matching Error, ξ (w.r.t. virtual, outside lens)	-	6.60×10^{-1}	4.29×10^{-1}	1.19
$w' = 12.7$ [λ]				
	Virtual Array	**Physical Array**		
Environment	Free-Space	Free-Space (No-SI)	Aniso-Lens (SI)	Iso-Lens (SI)
Number of elements	19	15		
Spacing [λ]	0.5	0.5		
Aperture [λ]	9.0	7.0		
$D_{\max}$ [dB]	14.73	13.71	14.27	13.44
SLL [dB]	13.06	13.08	12.79	12.13
$FNBW$ [deg]	12.07	15.31	12.97	15.67
$3dB$ Beamwidth [deg]	5.35	6.76	5.76	6.77
Matching Error, ξ (w.r.t. virtual, outside lens)	-	6.46×10^{-1}	4.57×10^{-1}	1.41
$w' = 13.3$ [λ]				
	Virtual Array	**Physical Array**		
Environment	Free-Space	Free-Space (No-SI)	Aniso-Lens (SI)	Iso-Lens (SI)
Number of elements	20	15		
Spacing [λ]	0.5	0.5		
Aperture [λ]	9.5	7.0		
$D_{\max}$ [dB]	14.96	13.71	14.23	13.03
SLL [dB]	13.18	13.08	12.52	16.42
$FNBW$ [deg]	11.44	15.31	12.88	28.90
$3dB$ Beamwidth [deg]	5.06	6.76	5.72	7.11
Matching Error, ξ (w.r.t. virtual, outside lens)	-	6.37×10^{-1}	5.55×10^{-1}	1.61

Table V: $\phi_s = 90$ [deg], $f = 600$ [MHz] - Final summary.

1.3.5 Final Summary: Performances vs. w' (vs. N')

Anisotropic Lens - $\phi_s = 90$ [deg]

This figure compares the pattern characteristics of

1. Original array ($N = 15$ elements, $d = \lambda/2$, Free-Space) - GREY;
2. Target array ($N' > N$ elements, $d = \lambda/2$, Free-Space) - RED;
3. QCTO-SI array ($N = 15$ elements, $d = \lambda/2$, Anisotropic Lens + SI) - CYAN;

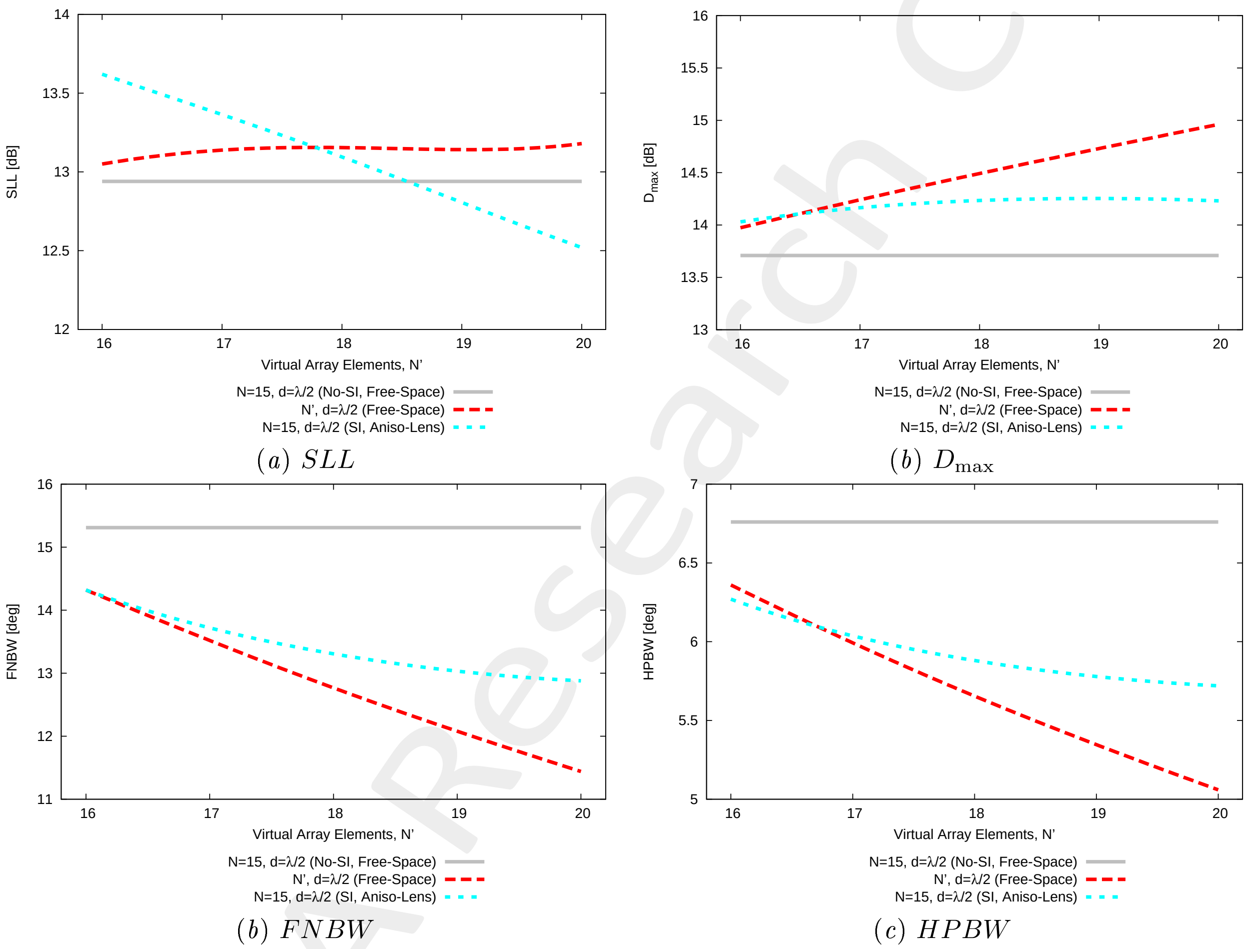

(a) SLL (b) $D_{\max}$

(b) $FNBW$ (c) $HPBW$

Figure 31: Aniso-Lens, $f = 600$ [MHz] - Pattern performances vs w' (vs. N').

2 Half-Cosine vs. Half-Gaussian Profile - Comparisons

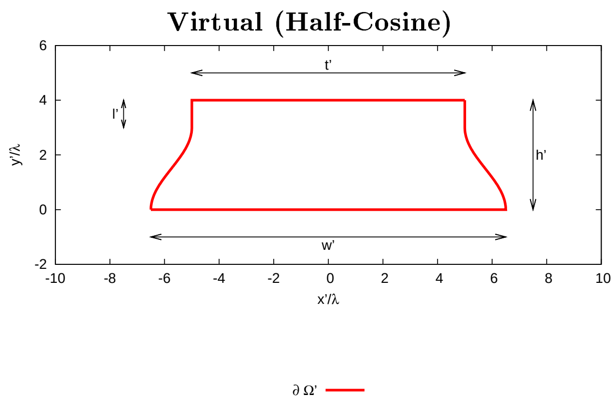

(a)

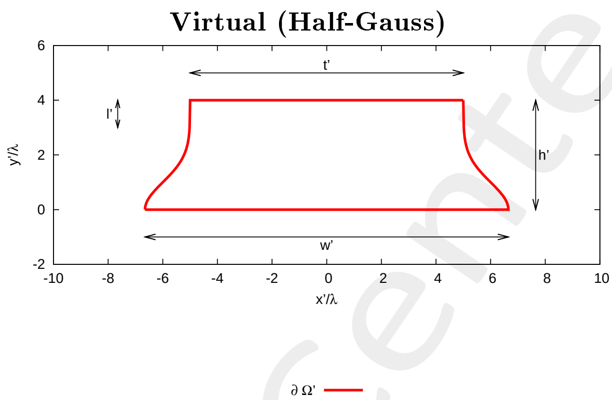

(b)

Figure 32: Transformation regions. The lower side of both virtual boundaries are supposed to be PEC.

Analyzed configurations

1. Half-Cosine profile

    - $h' = 4.0$ [λ], $l' = 1.0$ [λ], $t' = 10.0$ [λ], $N = 15$;

- Half-Gauss profile

    – $h' = 4.0$ [λ], $l' = 1.0$ [λ], $t' = 10.0$ [λ], $N = 15$;

2.1 Far-Field Patterns ($\phi_s = 90$ [deg], $f = 600$ [MHz]), After SI, Anisotropic Lens

Case $N = 15 \rightarrow N' = 20$

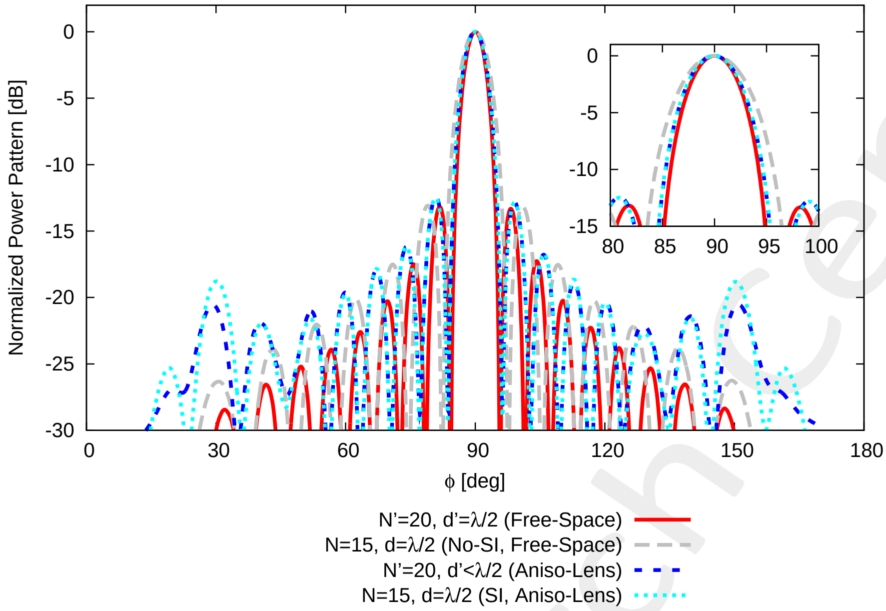

(a) Half-Cosine ($w' = 13.6$)

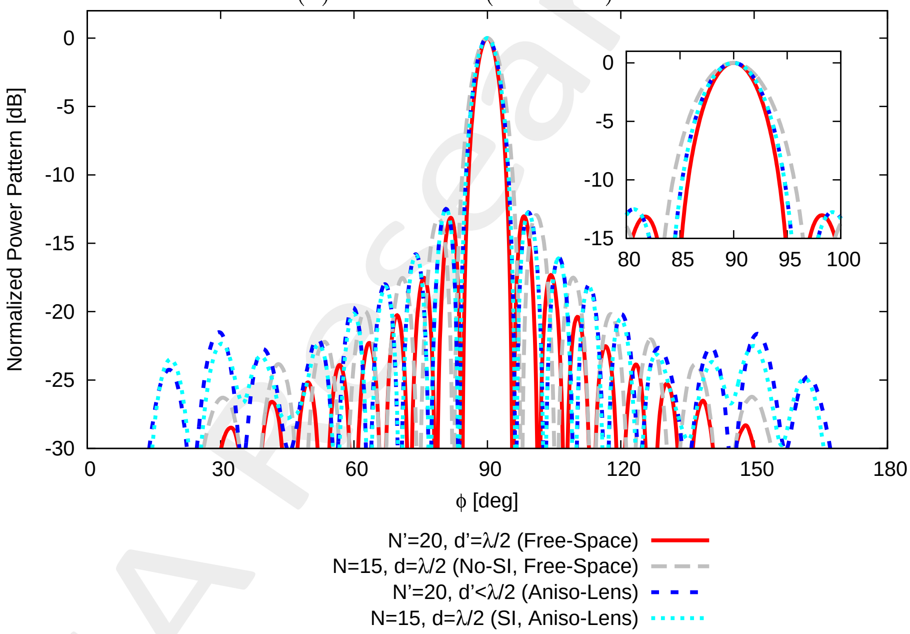

(b) Half-Gauss ($w' = 13.3$)

Figure 33: $\phi_s = 90$ [deg], $f = 600$ [MHz] - Far field pattern comparison after SI step.

Observations

- Using the same geometric parameters (i.e., h', l', t') the half-cosine profile provides slightly better results

References

[1] G. Oliveri, G. Gottardi, F. Robol, A. Polo, L. Poli, M. Salucci, M. Chuan, C. Massagrande, P. Vinetti, M. Mattivi, R. Lombardi, and A. Massa, "Co-design of unconventional array architectures and antenna elements for 5G base station," *IEEE Trans. Antennas Propag.*, vol. 65, no. 12, pp. 6752-6767, Dec. 2017.

[2] P. Rocca, G. Oliveri, R. J. Mailloux, and A. Massa, "Unconventional phased array architectures and design methodologies - A review," *Proc. IEEE*, vol. 104, no. 3, pp. 544-560, Mar. 2016.

[3] G. Oliveri, M. Salucci, N. Anselmi and A. Massa, "Multiscale System-by-Design synthesis of printed WAIMs for waveguide array enhancement," *IEEE J. Multiscale Multiphysics Computat. Techn.*, vol. 2, pp. 84-96, 2017.

[4] A. Massa and G. Oliveri, "Metamaterial-by-Design: Theory, methods, and applications to communications and sensing - Editorial," *EPJ Applied Metamaterials*, vol. 3, no. E1, pp. 1-3, 2016.

[5] L. Poli, G. Oliveri, P. Rocca, M. Salucci, and A. Massa, "Long-Distance WPT Unconventional Arrays Synthesis," *J. Electromagnet. Wave.*, vol. 31, no. 14, pp. 1399-1420, Jul. 2017.

[6] G. Oliveri, F. Viani, N. Anselmi, and A. Massa, "Synthesis of multi-layer WAIM coatings for planar phased arrays within the system-by-design framework," *IEEE Trans. Antennas Propag.*, vol. 63, no. 6, pp. 2482-2496, Jun. 2015.

[7] G. Oliveri, L. Tenuti, E. Bekele, M. Carlin, and A. Massa, "An SbD-QCTO approach to the synthesis of isotropic metamaterial lenses," *IEEE Antennas Wireless Propag. Lett.*, vol. 13, pp. 1783-1786, 2014.

[8] G. Oliveri, D. H. Werner, and A. Massa, "Reconfigurable electromagnetics through metamaterials - A review" *Proc. IEEE*, vol. 103, no. 7, pp. 1034-1056, Jul. 2015.

[9] G. Oliveri, E. T. Bekele, M. Salucci, and A. Massa, "Transformation electromagnetics miniaturization of sectoral and conical horn antennas," *IEEE Trans. Antennas Propag.*, vol. 64, no. 4, pp. 1508-1513, Apr. 2016.

[10] G. Oliveri, E. T. Bekele, M. Salucci, and A. Massa, "Array miniaturization through QCTO-SI metamaterial radomes," *IEEE Trans. Antennas Propag.*, vol. 63, no. 8, pp. 3465-3476, Aug. 2015.

[11] G. Oliveri, E. T. Bekele, D. H. Werner, J. P. Turpin, and A. Massa, "Generalized QCTO for metamaterial-lens-coated conformal arrays," *IEEE Trans. Antennas Propag.*, vol. 62, no. 8, pp 4089-4095, Aug. 2014.

[12] G. Oliveri, E. Bekele, M. Carlin, L. Tenuti, J. Turpin, D. H. Werner, and A. Massa, "Extended QCTO for innovative antenna system designs," IEEE Antenna Conference on Antenna Measurements and Applications (CAMA 2014), pp. 1-3, Nov. 16-19, 2014.

[13] G. Oliveri, P. Rocca, M. Salucci, E. T. Bekele, D. H. Werner, and A. Massa, "Design and synthesis of innovative metamaterial-enhanced arrays," IEEE International Symposium on Antennas Propag. (APS/URSI 2013), Orlando, Florida, USA, pp. 972 - 973, Jul. 7-12, 2013.

[14] G. Oliveri, "Improving the reliability of frequency domain simulators in the presence of homogeneous metamaterials - A preliminary numerical assessment," *Progress In Electromagnetics Research*, vol. 122, pp. 497-518, 2012.

[15] M. Salucci, G. Oliveri, N. Anselmi, G. Gottardi, and A. Massa, "Performance enhancement of linear active electronically-scanned arrays by means of MbD-synthesized metalenses," *J. Electromagnet. Wave.*, vol. 0, no. 0, pp. 1-29, 2017 (DOI: 10.1080/09205071.2017.1410077).